IR TC - 2125

MATERIALS RESEARCH FOR THE CLEAN UTILIZATION OF COAL

QUARTERLY PROGRESS REPORT

July - September 1980

Samuel J. Schneider
Project Manager

Center for Materials Science
National Bureau of Standards
U. S. Department of Commerce
Washington, D. C. 20234

PREPARED FOR THE UNITED STATES
DEPARTMENT OF ENERGY

Office of Advanced Research and Technology

Under Contract No. EA-77-01-6010

TABLE OF CONTENTS

PAGE

I. SUMMARY OF PROGRESS TO DATE

Brief Summary

1. Materials Performance and Properties

A contract for a computer vendor's services was awarded and conferences
held with the vendor to make a final choice of a Data Base Management
System. Plans for using the vendor's computer and receiving training
were laid. The first issue of the book on construction materials
for coal gasification nears completion.

2. Creep of MHD Refractories

Assembly of the 12 station creep facility was essentially completed;
system checkout has been started. Preliminary creep and tensile testing
on various refractories has been completed and analysis of data started.

3. Electrical Transport Mechanisms in Slag

Four probe AC electrical conductivity measurements are compared with
four probe DC measurements on slag from a coal burning steam plant in
Bow, NH. AC and DC data agree quite well with some anomalies existing
over the temperature range measured. The measurements support the
suggestion made in previous reports that above 1385 °C, ionic conductivity
is the predominant transport mechanism in this particular slag which
contains a relatively large amount of iron.

4. Corrosion of Downstream Components

Type 316 stainless steel tubes were exposed to an oxygen-rich and
fuel-rich environment seeded with K_2SO_4 and K_2CO_3. The samples
were maintained at 500 °C and 590 °C wall temperature using internal
air cooling. SEM and EDX analysis was performed on sections of the
samples showing the chemical nature of the reaction zone and salt
deposit. As seen in previous experiments, the Fe penetrates the salt
deposit to the greatest extent followed by lesser penetration by Cr
while Ni sometimes is found in the metal at the interface. In the
coming quarter the plans are to continue the study of Type 316 stain-
less steels using SEM-EDX analysis and to collect and analyze x-ray
diffraction data on residue salt deposit material from fuel-rich and
oxygen-rich systems. Also, the feasibility of using metal and ceramic
coatings on mild steel (with the testing of specific materials at
590 °C) will be examined.

II. DETAILED DESCRIPTION OF TECHNICAL PROGRESS

1. Materials Performance and Properties (H. M. Ondik, R. C. Dobbyn,
                                          A. Perloff, W. S. Brower,
                                          and W. A. Willard)

Progress: A contract for computer services was awarded to one of the
competing vendors at the end of July. Telephone and in-person confer-
ences have been held with the computer vendor to discuss plans for
setting up the computer data base. The merits and disadvantages of
several Data Base Management Systems (DBMS) were discussed. The vendor
prepared a sample data base for demonstration using a DBMS which appears
to have several advantages for easy search use. These advantages would
make the preparation of a users' manual simpler and help the outside
user of the data base. A definite decision has been made to use this
DBMS. In order to expedite the establishment of the data base the
vendor has offered extra assistance in transferring the Failure Infor-
mation Data Base to their computer as well as aid in the design of the
Materials Properties Data Base. Plans for training personnel in the use
of the vendor's computer and time-sharing services and the DBMS have
been made.

The Failure Information Center received four reports of detailed
failure analyses performed in DoE national laboratories. These reports
have been abstracted and encoded into the data base. The center also
received sixteen requests for information and data during the quarter.
In response to these requests a total of 2397 abstracts, several stat-
istical tables and nineteen hard copy reports were transmitted.

Work on the coal gasification construction materials book has
continued. Completed pages are being assembled, and further sections
are being prepared, including an index of materials and properties.

Plans: Data Center staff will be trained in the use of the vendor's
computer, time-sharing system, and the DBMS during the coming quarter.
The Failure Information Data Base will be transferred to the vendor's
computer, the Materials Properties Data Base will be designed, and
the keyboarding of input data will begin. The draft of the book on
construction materials for coal gasification will be delivered to DoE
for approval during the quarter.

2.   Creep and Related Properties of MHD Refractories (N. J. Tighe and
                                                        C. L. McDaniel)

Progress: During this quarter the creep and tensile tests were completed
on the excess magnesia-spinel (Corhart X-317) and the sodium doped alumina
(Carborundum Monofrax A) refractories. Experiments were conducted at
1400 °C, 1500 °C and 1600 °C; x-ray diffraction analysis of pre and
post test samples was performed. These data (mechanical properties and
phase composition) are now being analyzed and correlated; results will
be presented in the next quarterly.

Along with the experimental testing activity, significant effort also
was devoted to the assembly of the 12 station creep facility. The
recently delivered power supplies, however, apparently were damaged
in shipping and parts had to be returned to the manufacturer. Replace-
ments have been received and overall system checkout begun.

Plans: During the next quarter creep experiments will be started in
the 12 station creep assembly. A differential displacement device
will be evaluated for measuring the creep rate. Also, the reaction
of the sodium-doped material with slag (from the Montana State test rig)
will be evaluated and compared with the results obtained from the
creep tests. Additional samples will be obtained from Montana State
during a visit in October 1980. These will be selected from sections
of their air pre-heater during disassembly for inspection.

3. Electrical Conductivity and Polarization (W. R. Hosler)

Progress

Slag Electrical Conductivity

In the last quarterly report (April - June 1980), a detailed description of the sample preparation and measurement technique was presented. Figure 5 of the corresponding section of that report shows a radiograph of a typical slag sample with the leads attached and numbered. Figure 1 is a reproduction of that radiograph in this report for the convenience of the reader. The measurement technique and the data acquisition system has been extended to include the potential measurements between all probe sets, i.e. V_{12}, V_{23}, V_{34} and V_{14}. This has the advantage of being able to detect where polarization or abnormalities exist along the length of the sample with respect to the center of the sample. The center of the sample, monitored by probes 2 and 3, is the area where the bulk conductivity is measured and where it is assumed little or no polarization exists because no current is being drawn through the two contacts involved. This is because the potential between probes 2 and 3, as well as the other probe sets, is measured by a voltmeter whose input impedance is high compared to the sample resistance between those two probes. At the same time, current is introduced to the sample through probes 1 and 4, and it is at these areas where polarization and other effects may be observed. Consider the equation

$$f_{14}(V) = \frac{V_{12} + V_{23} + V_{34}}{V_{23} \, d_{14}/d_{23}} - 1 \qquad (1)$$

where d_{14} and d_{23} are the distances between probe 1 and 4 and between 2 and 3 respectively. The denominator of the first term in equation 1 is the potential between 1 and 4 normalized to the value between 2 and 3. This, of course, presumes that the cross-sectional area of the sample remains the same along the entire length of the sample. If it does not, these adjustments must be made in the normalization factor. If the value of equation 1 is zero or near zero, no polarization or inhomogeneities exist along the sample length except in the possible case that a deviation of V_{12} from the norm is equal to the negative deviation of V_{34} from the norm. This can be detected by use of the relationship:

$$f_{12}(V) = \frac{V_{12}}{V_{23}d_{12}/d_{23}} - 1 \qquad (2)$$

and

4

$$f_{34}(V) = \frac{V_{34}}{V_{23}d_{34}/d_{23}} - 1 \qquad\qquad (3)$$

which again represents the deviation from the norm of the potential value between probes 1 and 2 (equation 2) and between 3 and 4 (equation 3). If $f_{12}(V)$ and $f_{34}(V)$ are near zero, no polarization or inhomogeneities exist along the sample. If either or both of these values deviate widely from zero, polarization and/or inhomogeneities may exist. Figures 2 and 3 show plots of the values for equations 1, 2, and 3 for a slag sample measured with increasing temperature (Figure 2) and with decreasing temperature (Figure 3). This data was taken using a constant DC current and with equilibrium established at every point. This equilibrium was established by monitoring the potential value between probes 2 and 3 as a function of time. When this value changed over a period of 15 minutes by less than 1 percent, data for the temperature point was taken.

It is apparent that there are substantial differences between the curves for increasing and for decreasing temperatures below 1300 °C. This will be discussed later. It should be noted, however, that at temperatures above 1300 °C both figures show a marked increase in the f(V) values (with the exception of $f_{12}(V)$) which indicates an increase in the polarization effects because of enhanced ionic conductivity. Electric fields along the sample were kept at approximately 1 volt/cm in order to avoid possible permanent polarization. A more dramatic increase in the f(V) values would be observed using higher electric fields.

This result is in agreement with the argument set forth in several previous quarterly reports that above 1385 °C the conductivity in this particular coal slag (derived from ash products of a Bow, NH steam generating plant) is predominantly ionic.

AC Conductivity Measurements (Four probe)

At each equilibrated temperature AC conductivity measurements were made along with the DC measurements described above. The data at each temperature point was taken as a function of frequency from 40Hz to 40KHz. This limitation of frequency was imposed because of the AC voltage sensing instrument's limited frequency response. The accuracy over this frequency range was 0.3 percent of the reading plus 0.04 percent of the 10V range used. For these AC measurements, however, a constant current was not used. The AC signal generator output voltage was adjusted to obtain nearly one volt on the conductivity probes for every temperature point. The current was measured as the potential drop across a standard (adjustable) resistor in series with the sample. The data scans were made in the same sequence as in the DC case described previously.

Figure 4 shows the data at 40Hz for f(V) values of the equations 1, 2, and 3 for increasing temperature, while Figure 5 gives the data for decreasing temperature. Since this was the same sample as the DC case and measured at the same time, the sample conditions should be the same.

5

Below 1300 °C, the corresponding AC and DC curves are similar. Since
this is the case, it seems likely that the deviations from the near zero
values expected for an ideal sample with no polarization, cracks, or
inhomogeneities is caused primarily by inhomogeneities or microcracks.
Polarization effects would not show up in the AC data at 40Hz, but would
be apparent in DC data if ionic conductivity were prevalent.

On the other hand, there is a decided difference in the data for increasing
temperature compared to that for decreasing temperature and this difference
is evident for both DC and AC measurements. The reason for these differences
may be attributed to the difference in sample treatment. The relatively
rapid cooling of the sample from 1500 °C after the final filling process
before contacts were applied probably results in some microcracks as
well as some variation in crystalline components along the sample lengths.
These effects show up in the $f(V)$ data of Figures 2 and 4 differently
than the $f(V)$ data of Figures 3 and 5 where the sample was cooled very
slowly from high temperatures where microcracking should be a minimum.
It is interesting to note that $f_{34}(V)$ is negative and nearly constant in
Figure 5 over the entire temperature range below 1300 °C while $f_{12}(V)$
is positive and monotonically increasing as the temperature decreases.
This indicates that the condition of the sample in the volume between
probes 3 and 4 is not changing appreciably as the sample is cooled, but
in that volume between probes 1 and 2 it is changing. Under this situation,
an analysis of the two ranges under a scanning electron microscope might
reveal the nature of the different behaviors. This also demonstrates a
case where a negative $f_{34}(V)$ partially compensates for a positive $f_{12}(V)$
and gives a $f_{14}(V)$ value nearer zero than it should be. The conclusion,
is, that since the AC and DC data are in relatively close agreement,
polarization effects do not play a large role in the measurements and
the conductivity in this temperature range is not predominantly ionic in
nature.

Figure 6 is a plot of the conductivity as a function of frequency for
the data taken with increasing temperature points while Figure 7 is the
same data taken with decreasing temperature. The increase in conductivity
with increasing frequency at lower temperature in each case may be due
to the capacity of the twisted lead pair from the sample to the data
acquisition system. A rough calculation of this capacity leads to an
impedance value at 40KHz of the same order of magnitude as the resistance
observed between the conductivity probes. A room temperature measurement
of the capacitative reactance of the lead pairs has confirmed this calculation.

At temperatures above 1300 °C, the 40Hz AC data shown in Figures 4 and 5
remain near zero in contrast to that data for the DC case (Figures 2 and
3). Polarization effects are not observed at 40Hz or over the frequency
range measured and as a result, the $f(V)$ values remain near zero.

Figure 8 shows the AC (40Hz) and DC conductivity taken with increasing
temperature. The maximum at about 1100 °C and the minimum at 1150 °C
are distinct although the AC and DC values at the minimum differ by nearly a
factor of two. They are in near exact agreement, however, above 1385 °C

where ionic conductivity is predominant and nearly equal below 1000 °C
where the slag is solid and electronic conductivity is probably predominant.

Figure 9 shows the AC (40Hz) and DC conductivity as a function of decreasing
temperature. In this case, there is only an inflection point near
1150 °C and the AC and DC values differ again by about a factor of two.
Since for both the increasing and decreasing temperature curves (Figure
8 and 9) careful attention was paid to obtaining equilibrated values,
the reason for the difference in the curve shapes with increasing and
decreasing temperatures is not clear. This should be investigated by
SEM methods in an effort to determine the sample conditions under the
two different situations.

It should be pointed out that previous electrical conductivity measure-
ments on coal slag reported in previous quarterly reports were done by
quenching the sample from some temperature above the softening point to
a temperature (900 °C) below the softening point in order to quench in
an established Fe^{+2}/Fe^{+3} ratio at lower temperature. These measurements
were taken under equilibrated conditions so that the Fe^{+2}/Fe^{+3} ratio
could change depending on the temperature at least above 900 °C.

From the results described above, obtained by the methods of measurements
and sample preparation techniques described previously, it is possible
to arrive at certain conclusions about sample condition during the
course of the measurement. These conclusions are stated in the text.
The main result is, however, that these measurements support the viewpoint
stated previously that the electrical conductivity of slag from coal
burned at the Bow, NH plant is predominantly ionic above 1385 °C. In
addition, these measurements demonstrate that four probe DC measurements
are valid for obtaining a bulk conductivity of ionic conductors providing
certain conditions are met.

Plans: The electrical conductivity work reported over the last year has
been on slags containing relatively large amounts of iron. These
measurements will be extended to those slags containing less iron and
more calcium typical of slags from Western coals. SEM investigations
will be started in an effort to understand some of the anomalies described
in the text of this report.
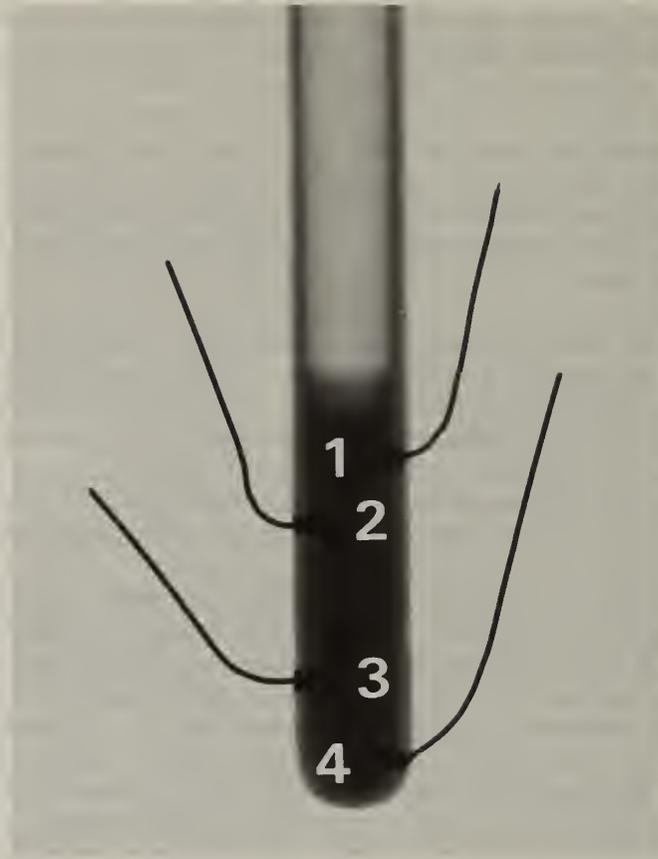
Figure 1. Radiograph of a typical slag sample. Platinum probes 1, 2, 3, and 4 are shown with probes 2 and 3 being the conductivity pair; and probes 1 and 4, the pair where current is introduced to the sample.
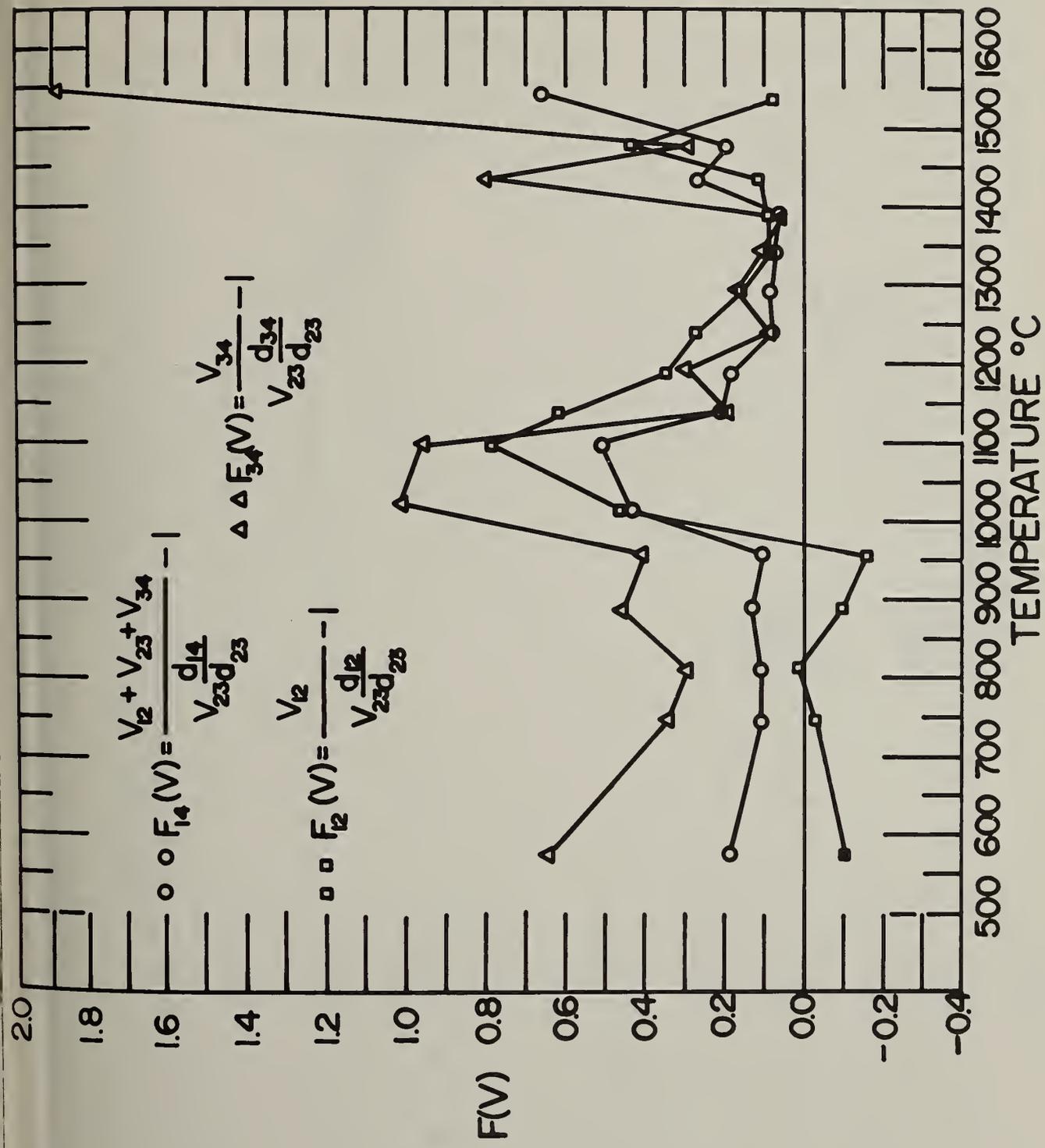
Figure 2. Plot of the DC values for equations 1, 2, and 3 as a function of temperature for increasing temperature.
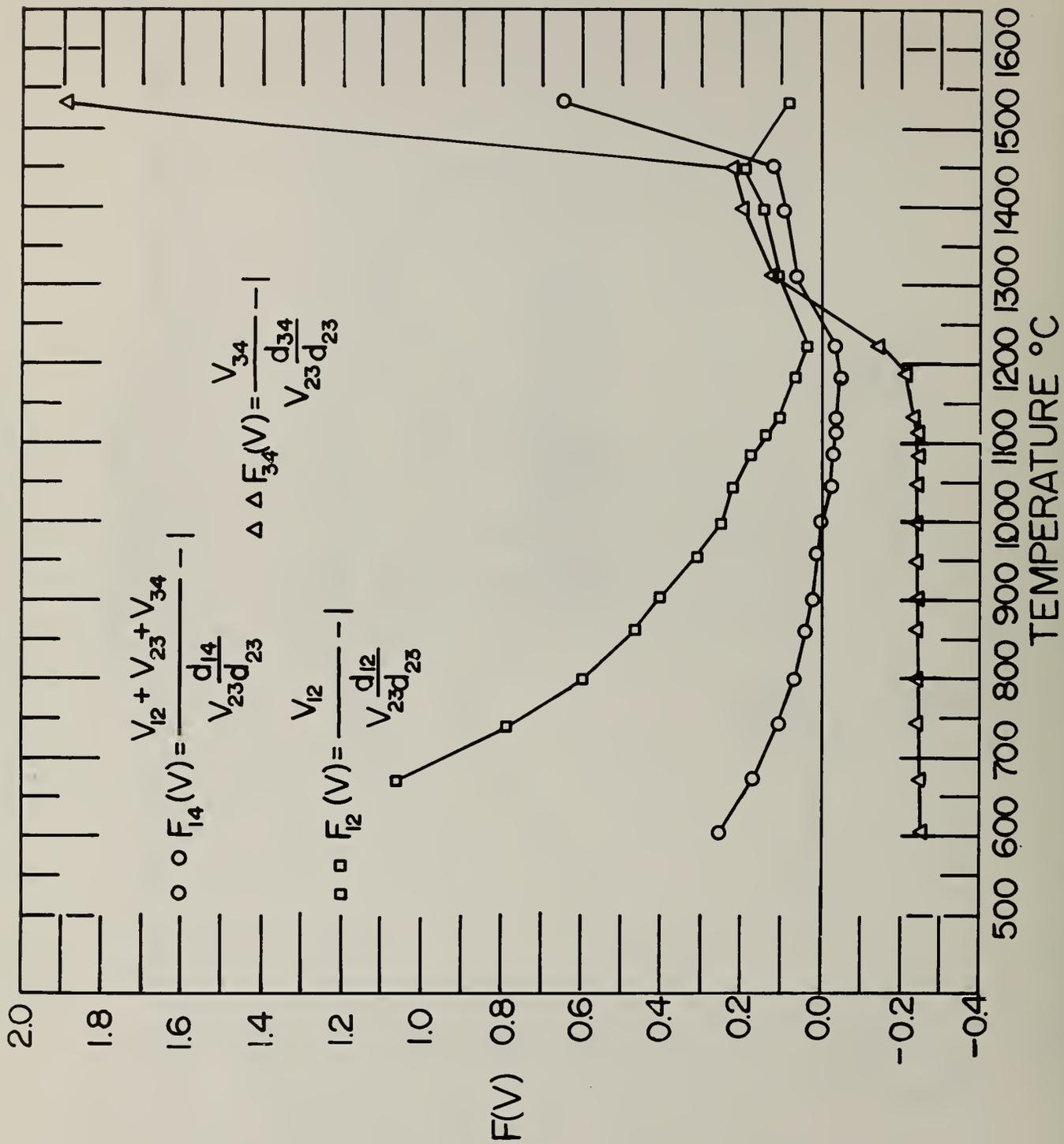
9

Figure 3. Plot of the DC values for equations 1, 2, and 3 as a function of temperature for decreasing temperature.
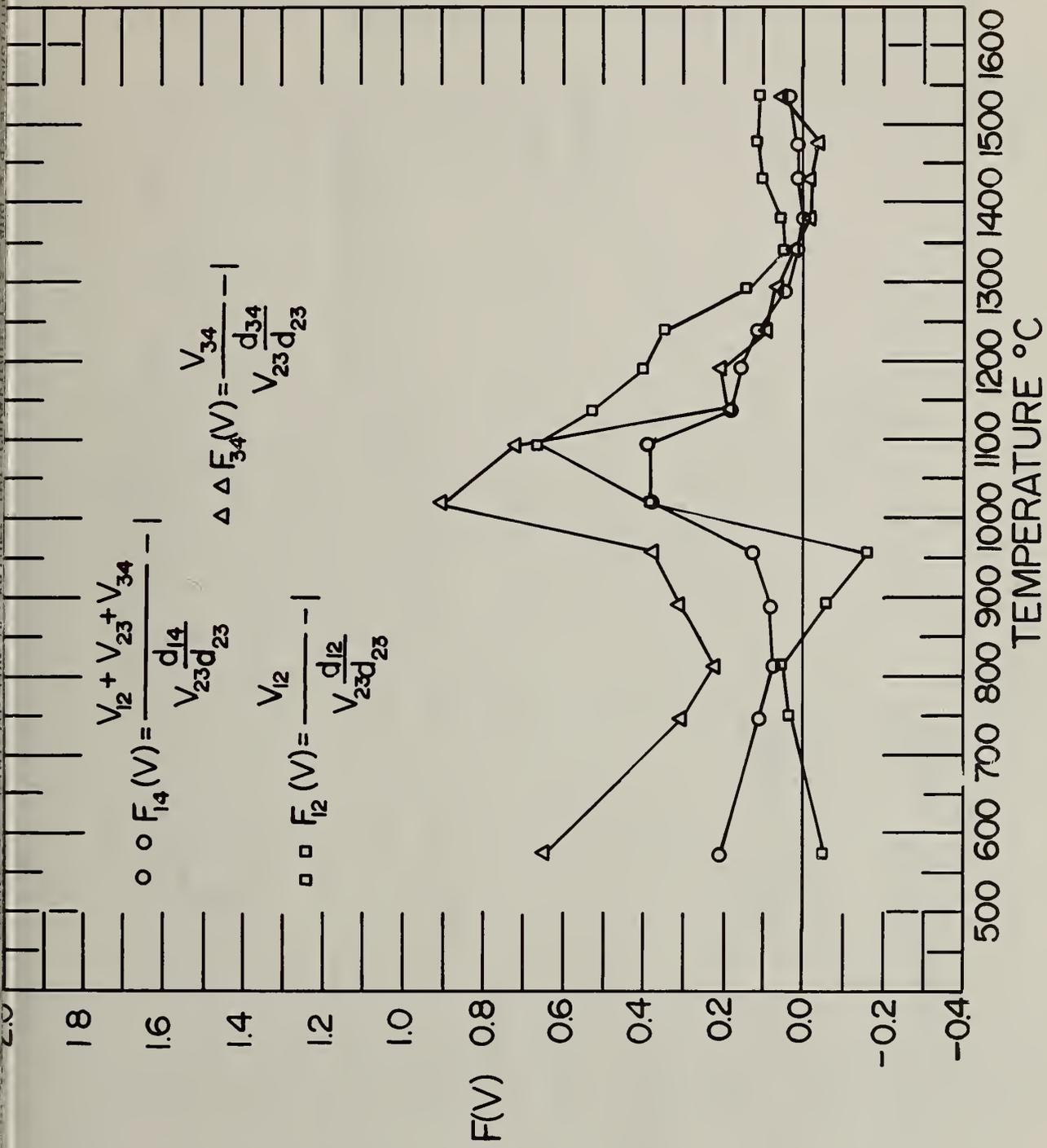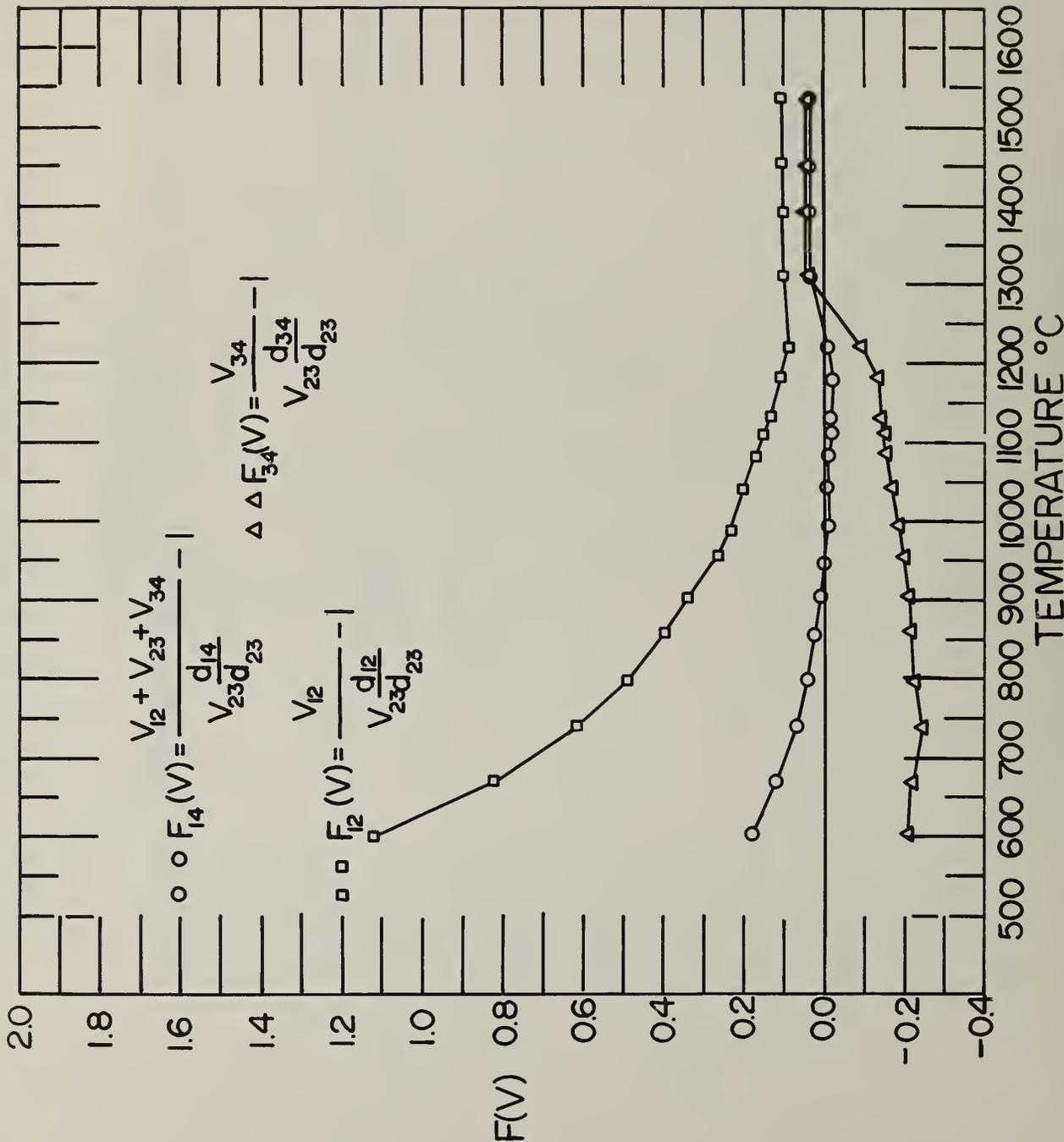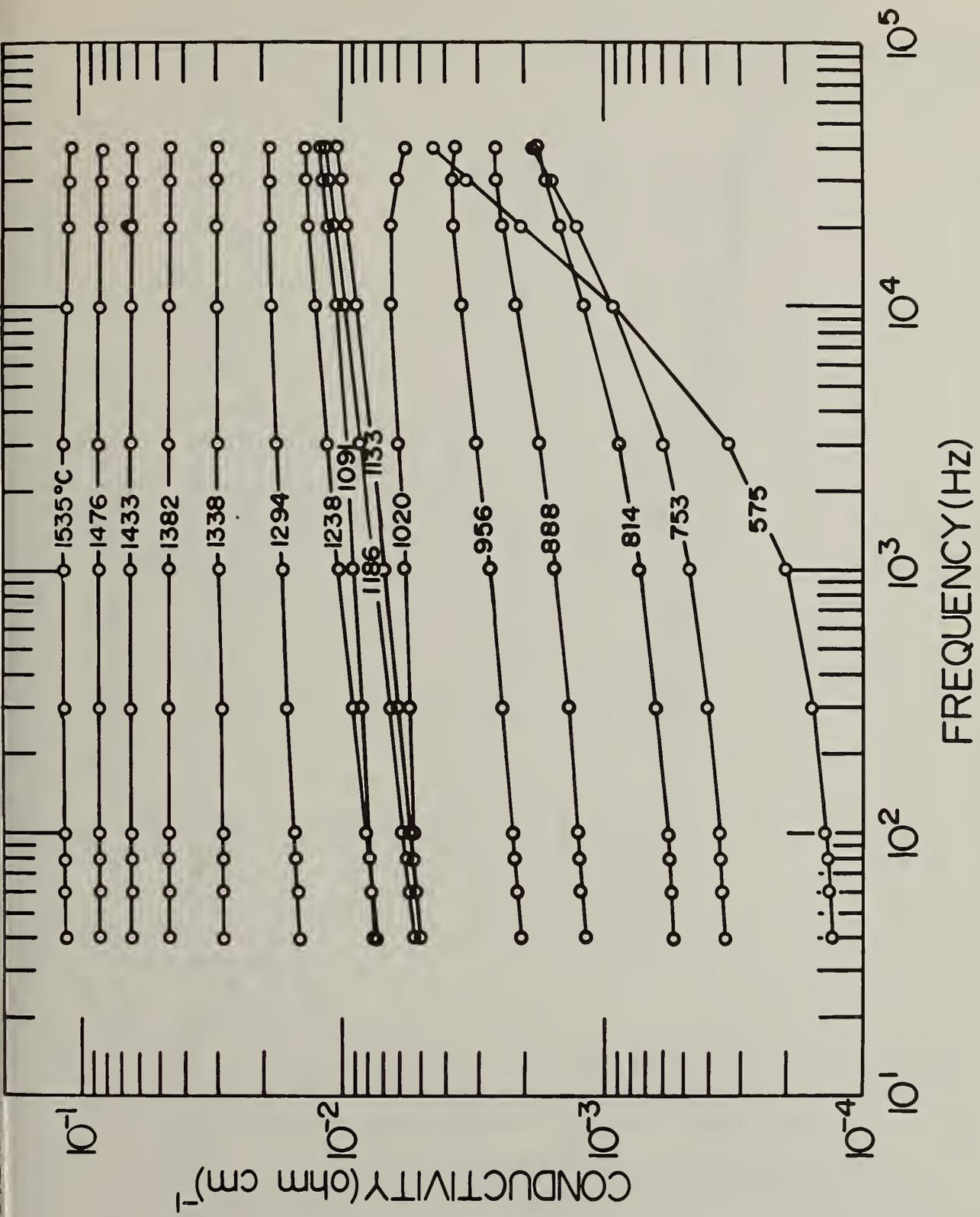
$$\circ \circ F_{14}(V) = \frac{V_{12} + V_{23} + V_{34}}{V_{23} \frac{d_{14}}{d_{23}}} - 1$$

$$\triangle \triangle F_{34}(V) = \frac{V_{34}}{V_{23} \frac{d_{34}}{d_{23}}} - 1$$

$$\square \square F_{12}(V) = \frac{V_{12}}{V_{23} \frac{d_{12}}{d_{23}}} - 1$$

F(V)

TEMPERATURE °C

500 600 700 800 900 1000 1100 1200 1300 1400 1500 1600

18 16 14 12 10 0.8 0.6 0.4 0.2 0.0 -0.2 -0.4

Figure 4.   Plot of 40Hz AC values for equations 1, 2, and 3 as a function of temperature for increasing temperature.

11

Figure 5. Plot of 40Hz AC values for equations 1, 2, and 3 as a function of temperature for decreasing temperature.

$\circ \circ F_{14}(V) = \dfrac{V_{12} + V_{23} + V_{34}}{V_{23}\frac{d_{14}}{d_{23}}} - 1$

$\triangle \triangle F_{34}(V) = \dfrac{V_{34}}{V_{23}\frac{d_{34}}{d_{23}}} - 1$

$\square \square F_{12}(V) = \dfrac{V_{12}}{V_{23}\frac{d_{12}}{d_{23}}} - 1$

TEMPERATURE °C

500 600 700 800 900 1000 1100 1200 1300 1400 1500 1600

F(V)

2.0 1.8 1.6 1.4 1.2 1.0 0.8 0.6 0.4 0.2 0.0 -0.2 -0.4

12

Figure 6. Conductivity as a function of frequency over a range of increasing temperatures.

13
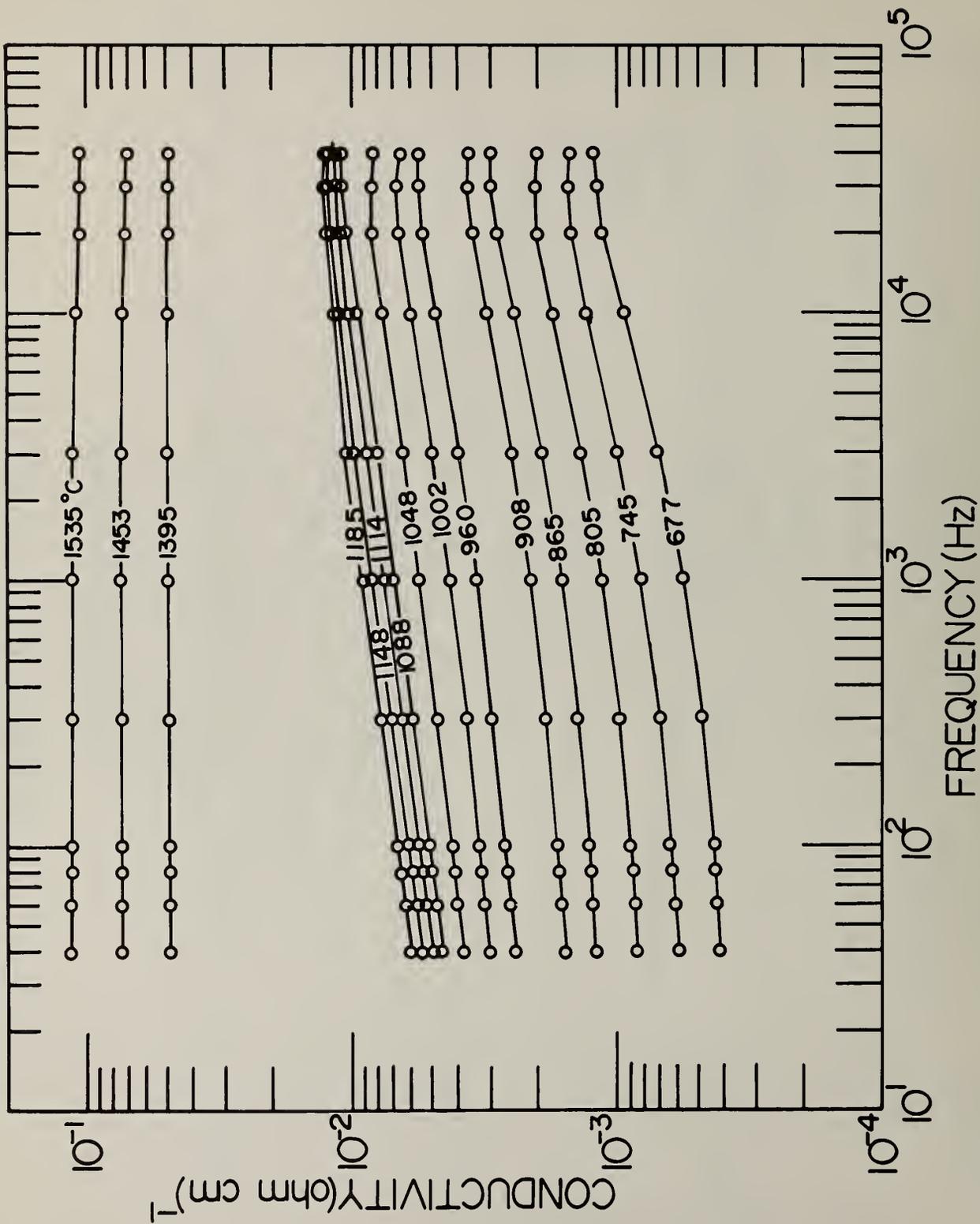
Figure 7. Conductivity as a function of frequency over a range of decreasing temperatures.
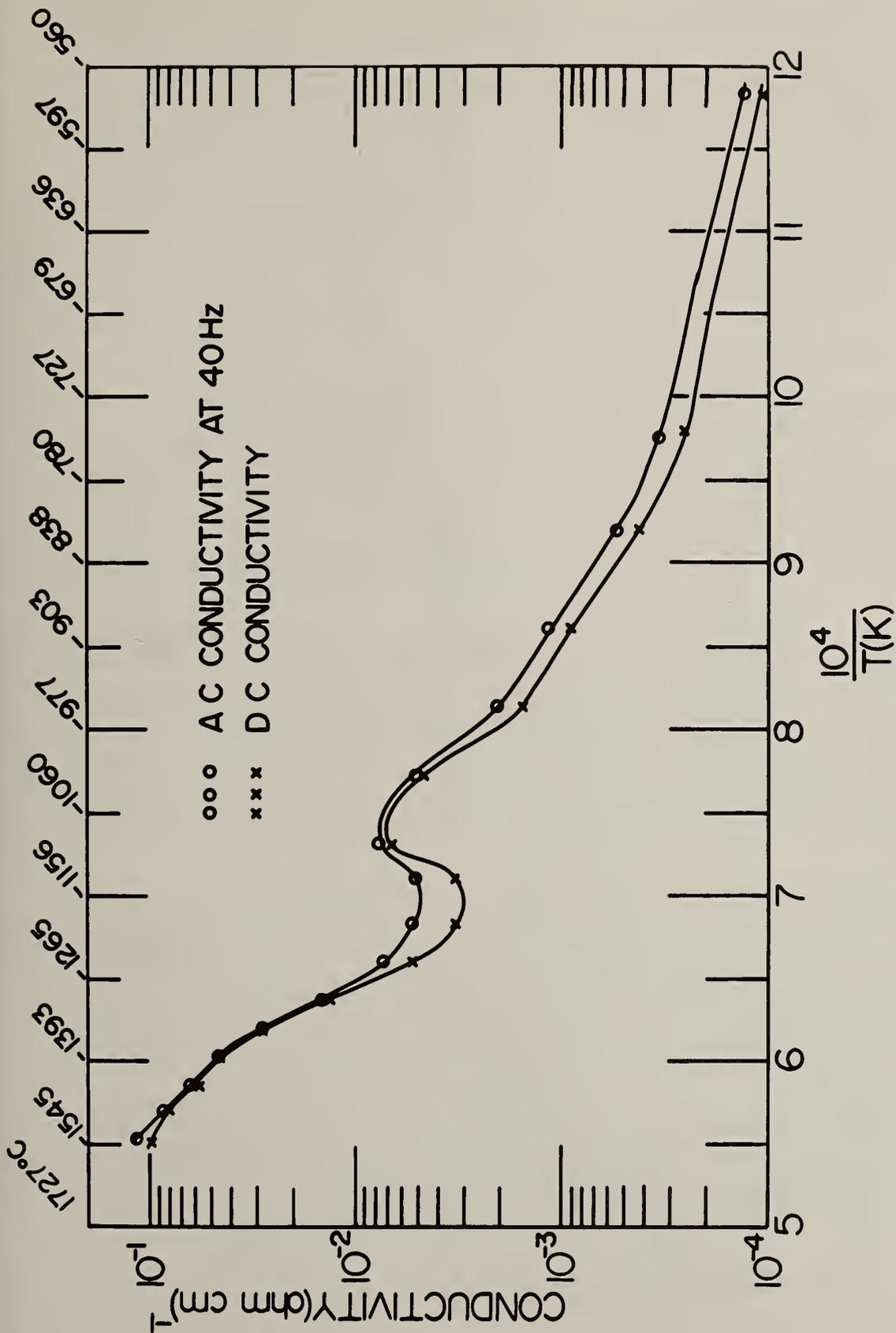
Figure 8. DC and 40Hz conductivity as a function of increasing temperature after sample preparation.
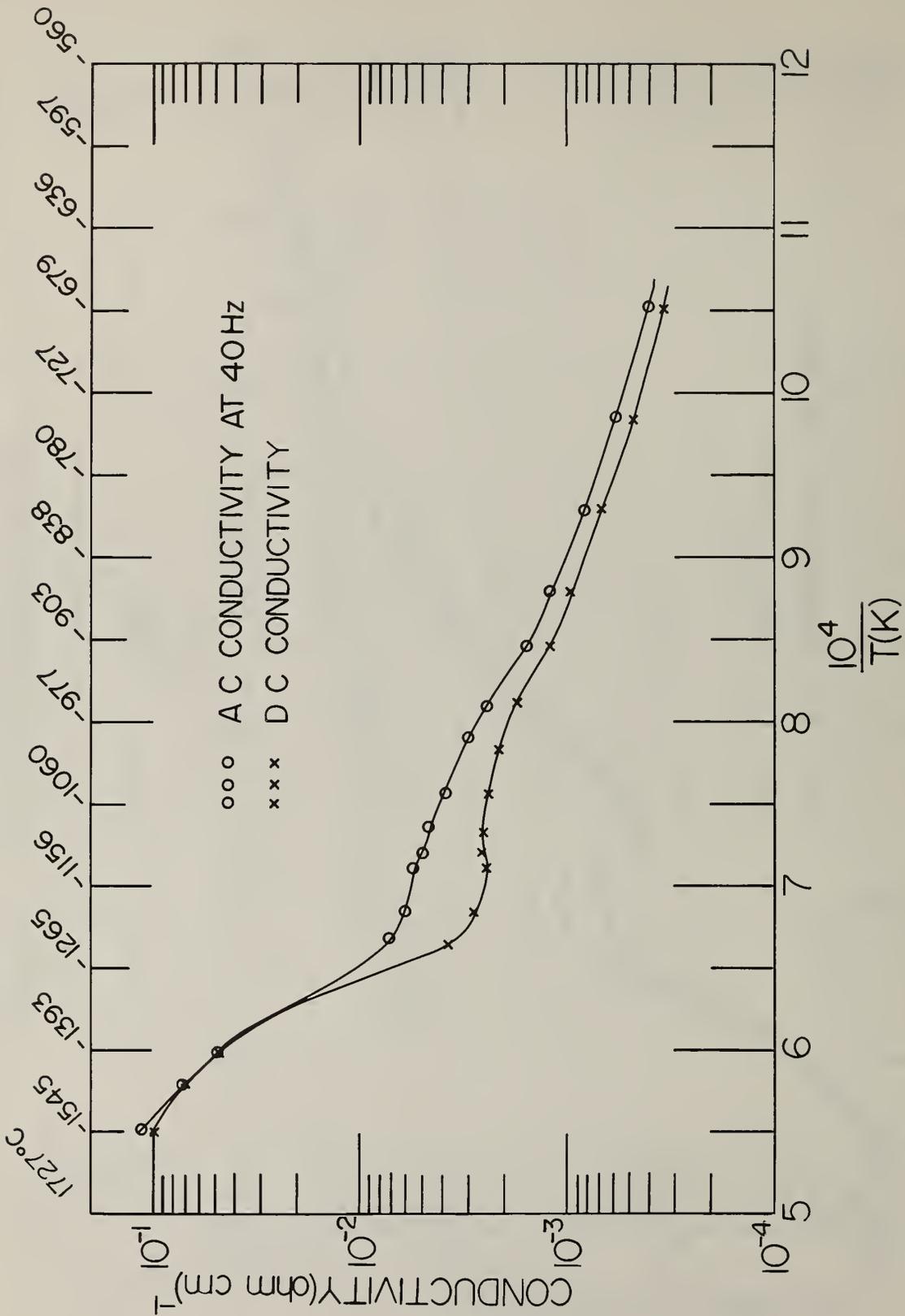
Figure 9. DC and 40Hz AC conductivity as a function of decreasing temperature from above 1500 °C.

4. Corrosion of Downstream MHD Components (J. Smit and C. D. Olson)

Progress: Exposure of tubular specimens, Type 316 stainless steel, were performed under varied conditions of K_2SO_4, K_2SO_4-K_2CO_3 seed and oxygen rich or propane rich hot gas streams. All samples were exposed, exclusive of apparatus warm up and cool down, for a period of approximately four hours with seeding of 250 g of salt occurring in the first 25 minutes. Four stainless steel specimens were exposed under these general conditions, three at 590 °C and one at 500 °C. The sample temperatures were maintained using air to internally cool the tubular walls and the wall temperature was monitored using Pt/Pt-10%Rh thermocouple welded into the wall at the mid-length point. The gas stream temperature, in all cases, was held at approximately 1300 °C as indicated by a Pt/Pt-10%Rh thermo-couple placed in the vicinity of the test specimen. The test specimens, following the exposure runs, were analyzed using SEM/EDX.

SEM/EDX Analysis of the Metal-Salt Deposit Interface - Test specimens were removed from the test rig upon cool down to approximately 40 °C and encapsulated immediately in epoxy to prevent any possibility of contamination and to reduce the possibility of hydration occurring in the salt coatings. Metallographic specimens were selected from the tubular specimen, 10 mm from the mid-length point. The specimens were cut, ground, and polished using non-aqueous media and stored in evacuated desiccators prior to SEM/EDX analysis.

Test specimens numbers 8-6, 9-6, and 6-6 were exposed at 590 °C and number 5-6 was exposed at 500 °C. All specimens exhibited similar salt deposit characteristics. The surface facing the gas stream was thinner than the deposit on the side portion of the tube (drip zone), and a thin fume deposit was found on the underside of the tube. The thickness of the top surface deposit was found to be consistent with previous samples in that, the surface salt deposit is thinner as the wall temperature increases. Also, under fuel rich conditions the deposit is thinner than in the oxygen rich environment.

An evaluation of specimens 8-6 (Figure 1) and 9-6 (Figure 24) can be made simultaneously. Both samples were seeded with 80% by weight K_2CO_3 and 20% by weight K_2SO_4, with wall temperatures of 590 °C, however, 8-6 was in an oxygen rich fuel environment and 9-6 was in a fuel rich environment. The variations in the salt deposit can readily be observed with the oxygen rich specimen (8-6) exhibiting a top deposit of 0.3 mm, drip deposit of 2 mm and a slight fume deposit. The fuel rich specimen (9-6) shows a top coating of 0.1 mm, drip deposit of 1.6 mm and a very unusual fume deposit region, dendritic in nature. Photos (Figures 2 and 3) show a banding property in the deposit with K + S near the surface of the steel followed by a high K region with a thin band of K + S on the surface. This phenomenen is also seen in the

fuel rich specimens coating. The bulk of both coatings, however, is generally high in potassium (K) with moderate to low amounts of sulfur (S) found.

The corrosion process exhibited in both specimens seem to follow the same general corrosion mechanism. In sample 8-6 (oxygen rich) at the leading edge, salt-stainless interface (Figures 1, 4-12) we find the bulk stainless followed by a reaction zone area where high nickel is found with chromium and iron followed by an area of high chromium, high iron, nickel and potassium. Chromium and iron are then found penetrating the salt deposit with the iron being the most mobile species and moving far into the salt deposit. Nickel being the least mobil or least reactive species is generally not found to penetrate the salt deposit except at the interface where chromium and iron move rather readily through the salt.

In 8-6 (Figure 13), the corrosion or reaction zone can be seen at the drip zone salt deposit stainless steel interface region. This darker band region, as analyzed using EDX, Figures 13-20, shows high chromium, iron, low nickel, and potassium, indicating a reacted area on the metal surface. Analysis above and below this region again shows cation mobility. We find concentrations of the cations as follows: a) bulk stainless steel, b) higher nickel-chromium-iron, c) higher chromium-iron-nickel-potassium, d) chromium-high iron-potassium, e) iron-potassium, f) high potassium. Traces of sulfur are found in the coating and reaction areas, also, indicating some sulfur-cation reaction. Therefore, the SEM/EDX analysis seems to indicate a preferential leaching of the metal cations from the bulk materials (Type 316 stainless steel) in a somewhat orderly fashion as in the case of the 304 stainless steel. This can be corroborated by wastage (weight loss) experiments described in previous reports. The chromium and iron cations appear to be the more reactive species in the stainless steel and are preferentially leached by the potassium-sulfur salt. As these cations migrate from the bulk stainless steel composition to the salt deposit the relatively non-reactive nickel is left and what appears as layering is observed.

Figures 21-23 shows a portion of the fume deposit region where the corrosive process appears to be evident. On the edge, areas of low nickel are found, while areas of chromium, iron, potassium, and sulfur are found in the reaction zone. However, in the fume deposit region there is not as great a separation of the cations, as found by EDX, possibly due to the fact that no direct contact of the salt is made in this area during deposit but rather collected on the underside by condensation from the vapor.

In sample 9-6, fuel rich, at the leading edge of the stainless steel (Figures 24-34) we again find the bulk stainless steel followed by a reaction zone area. As in the fuel rich sample (8-6), what appears to be a distinctive corrosion banding appears using EDX analysis. The corrosive process in the oxygen rich fuel environment

appears to follow the same general pattern as found in the fuel rich environment. The cations are found again in a general order of mobility where: a) bulk stainless steel, b) higher nickel-high chromium-iron, c) chromium-iron-nickel-potassium, d) chromium-higher-iron-potassium e) iron-potassium, f) high potassium. Again sulfur is found in small amounts in the reaction zone area and coating.

In the fuel rich environment the reaction zone area does not appear to be as distinct as in the oxygen rich environment. The fuel rich system shows no areas of high nickel above the bulk stainless steel but shows high nickel associated with high chromium. There is, in general, more sulfur present when higher nickel is found, possibly forming nickel-sulfur compounds. As shown previously in the oxygen rich environment, the fuel rich environment shows that chromium and iron are the most mobile cation species that penetrate the salt deposit.

The drip zone region also exhibits a reaction band area in the fuel rich system. The same corrosion process is observed in this area as previously describe for the top of the tube. The fume deposit region examined exhibits a reaction zone area while the salt deposit shows high potassium content. Again iron and some chromium is found in the fume deposit, indicating the relative ease for these cations to migrate.

In sample 6-6, the tube wall was maintained at 590 °C but the corrosive salt used was K_2SO_4 in a fuel rich environment. As found in previous fuel rich systems the coating was thin on the leading edge of the tube, 0.1 mm, while the drip zone region built up, 1 mm. The fume deposit exhibited an unusual formation of material build up similar to what was observed in 9-6. The coating appears to have a more columnar nature which has been observed with previous samples using K_2SO_4 salt exclusively.

The reaction zone area in 6-6 (Figures 35-43) is not well delineated in the fuel rich system as compared to the o ygen rich system, however, corrosion is observed. SEM/EDX analysis indicated that the reaction bands above the stainless steel bulk composition have the following sequence: a) low chromium-nickel-iron, b) high chromium-iron-no nickel, c) chromium-iron-potassium, d) high potassium-chromium-iron, e) high potassium-iron, f) high potassium. Traces of sulfur are associated with the potassium but the bulk of the salt coating is high in potassium. As found in previous specimens, nickel is absent in high concentration. At the interface no nickel is detected whether this be through loss of the nickel or its displacement to other areas not readily detectable is not apparent. However, the migration of chromium to the edge of the stainless steel is seen with iron and chromium penetrating the salt deposits. Examination of the drip deposit region show similar results as previously discussed with the absence or near absence of nickel at the metals edge, and with chromium and iron moving into the salt layer region. The fume deposit region showed minimal corrosion while the coating contained high potassium.

At a lower temperature of 500 °C, corrosion is still observed in Type 316 stainless steel, 5-6, using K_2SO_4 salt in a fuel rich environment. Figures 44-49 shows the reaction zone area at the metal-salt interface at the leading edge. In this area we find, using SEM/EDX: a) bulk stainless steel, b) low nickel-high chromium-iron-potassium-sulfur, c) potassium-iron-chromium-sulfur, d) potassium-iron-sulfur, e) potassium-sulfur. An area of high nickel is not detected while areas of high chromium and iron are readily discernible in the reaction zone. This corrosion mechanism is also found in the drip zone area and the fume deposit region, though both to a lesser degree.

Conclusion: The variances between fuel rich and oxygen rich environments in the presence of K_2SO_4 and K_2CO_3 are minimal. Corrosion of the Type 316 stainless steel seems to occur readily in both instances. The oxygen rich system, however, does seem to exhibit a more definable corrosion band area than the fuel rich system. Both systems show that iron and chromium are the more mobile species and that nickel is relatively unreacted. In the oxygen rich system the nickel can be followed from the bulk composition to the interface due to the migration of iron and chromium upwards from the bulk to the surface and then into the coating. In the fuel rich system nickel does not seem to be left behind or found in high concentrations even though iron and chromium are found to migrate into the salt deposit. In previous samples, nickel was found infrequently, but localized, in high concentrations in the high chromium region.

In general, therefore, both systems indicate the same metal cation movement from the bulk stainless steel into the salt deposit.

Plans: 1) Continue the study of Type 316 stainless steel using SEM/EDX analyses, 2) analyze collected x-ray diffraction data of residue salt deposit material from fuel rich and oxygen rich systems, and 3) examine the feasibility of using ceramic and metal coating on mild steels with testing of specific materials at 590 °C.

Fig. 1.   Optical micrograph of a section of Type 316 stainless steel tubing after exposure to an oxygen rich hot gas stream seeded with K_2SO_4 and K_2CO_3. Tube temperature 590°C.   Note deposit on upper surface of tube.

Fig. 2.   SEM micrograph, 45 X, of region T of optical micrograph Fig. 1 showing metal-salt deposit interface in the drip zone.

21

Fig. 3.   SEM micrograph, 92 X, of region T of optical micrograph Fig. 1 showing
           metal-salt deposit interface in the drip zone.

Fig. 4.   SEM micrograph, 5460 X, of region]Z of optical micrograph Fig. 1 showing
           reaction area at metal-salt interface. Lettered regions correspond to
           labeled EDX spectra Fig. 5-12.
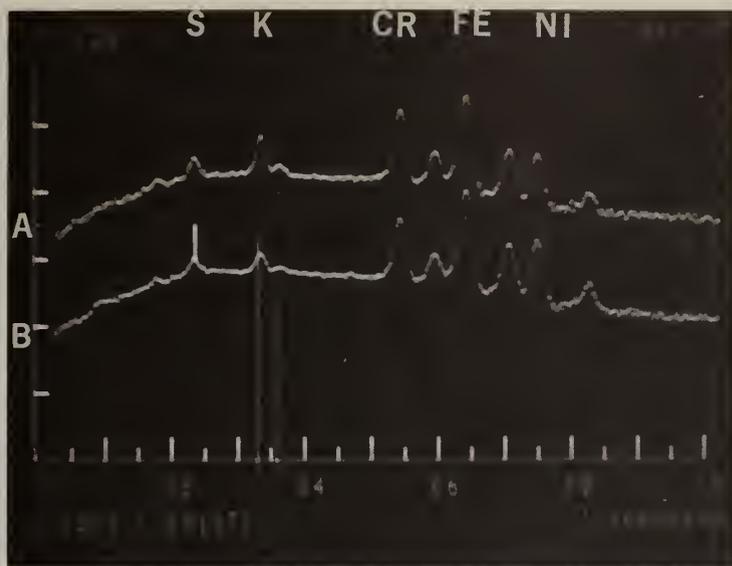
Fig. 5.   EDX spectra of regions A and B of Fig. 4 showing slight increase
in Ni concentration at metal-reaction zone interface (spectrum B).
Specie position and designations of all spectra in this section
of the report are as indicated above.
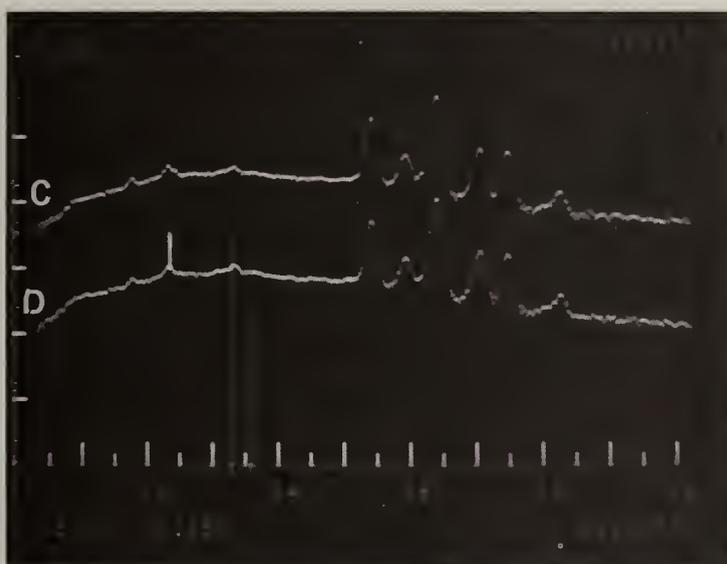
Fig. 6.   EDX spectra of regions C and D of Fig. 4 showing bulk spectra.
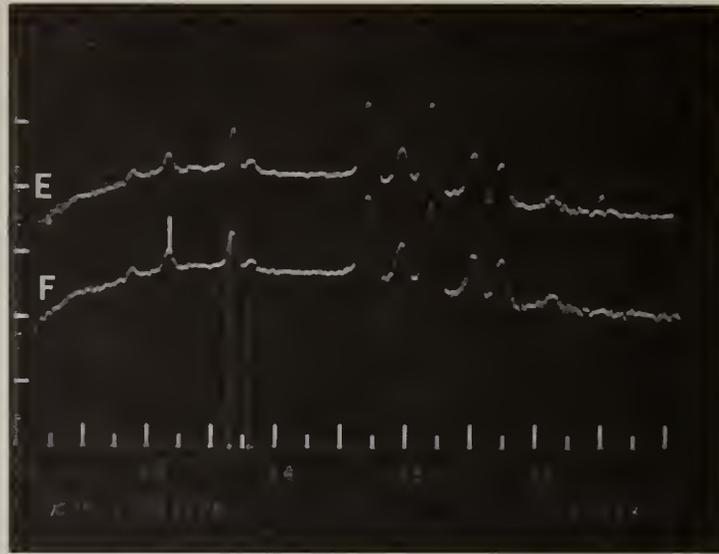
Fig. 7. EDX spectra of regions E and F of Fig. 4 showing high concentrations of Cr.
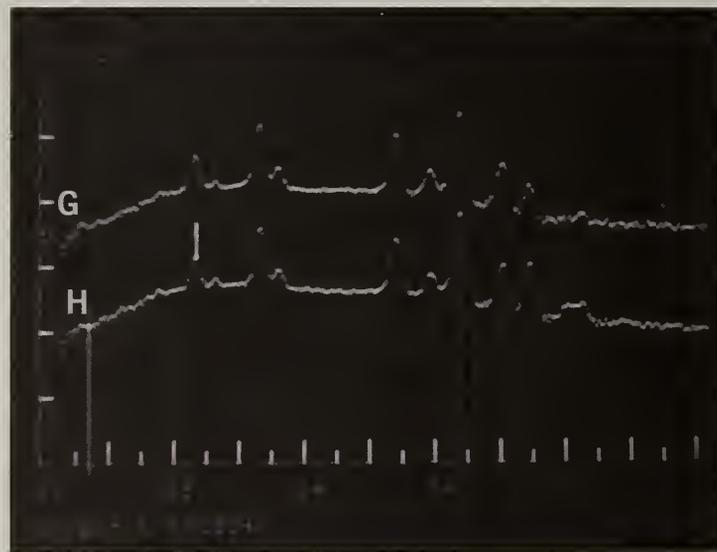
Fig. 8. EDX spectra of regions G and H of Fig. 4 showing low concentration of Ni.
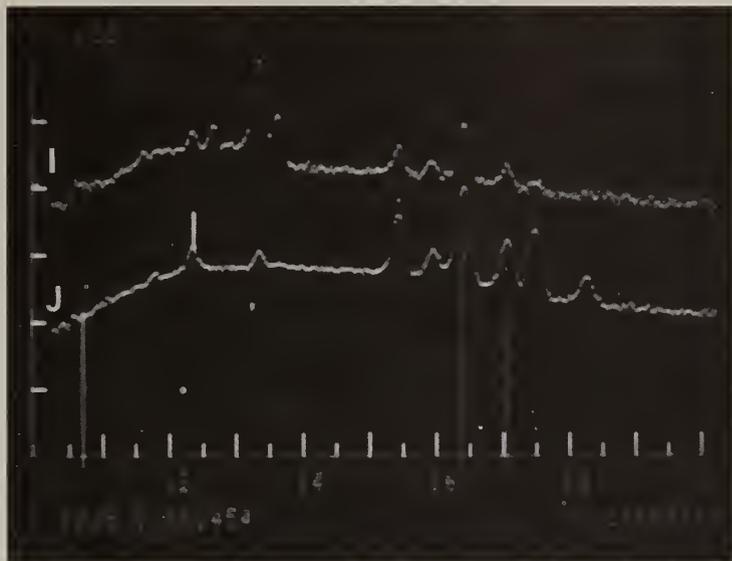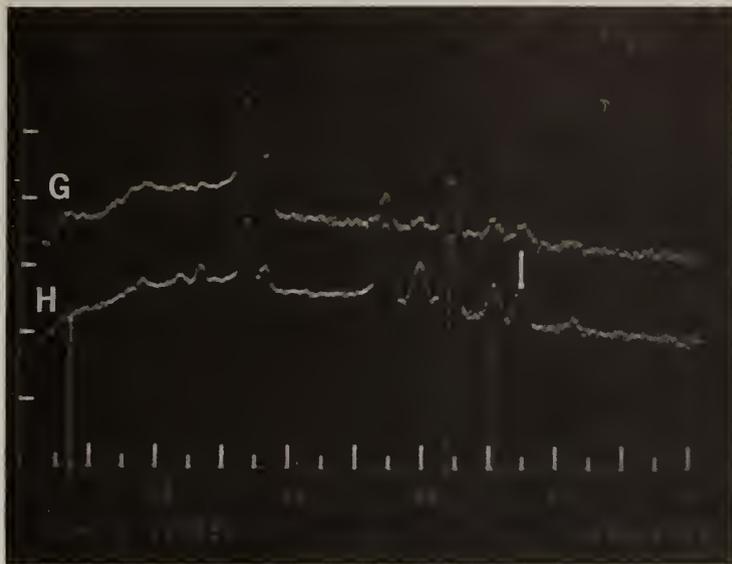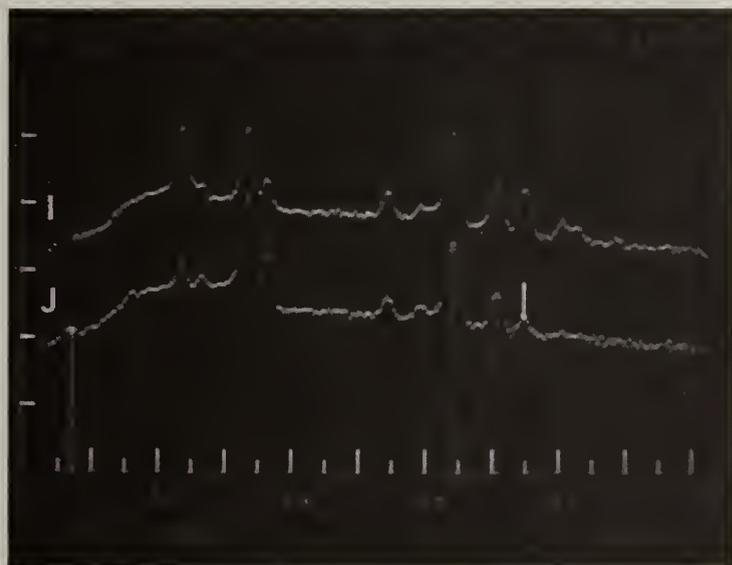
Fig. 9. EDX spectra of regions I and J of Fig. 4 showing high concentrations of K.
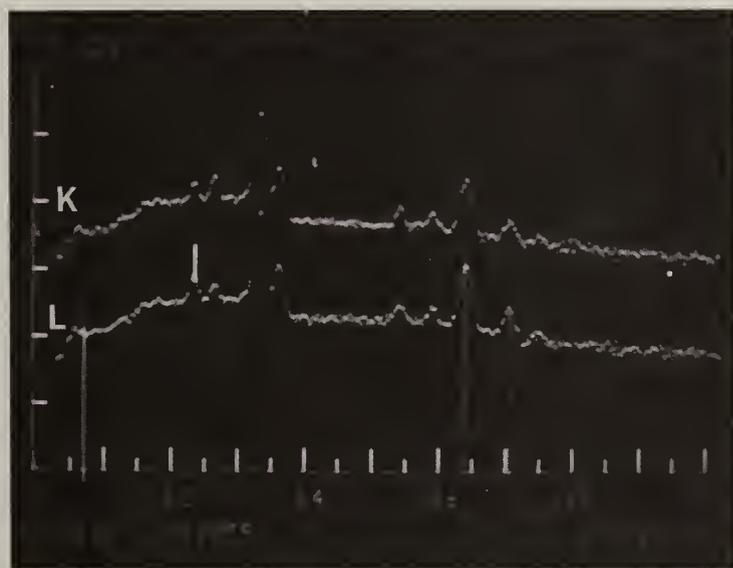
Fig. 10. EDX spectra of regions K and L of Fig. 4 showing high Fe and K concentrations.
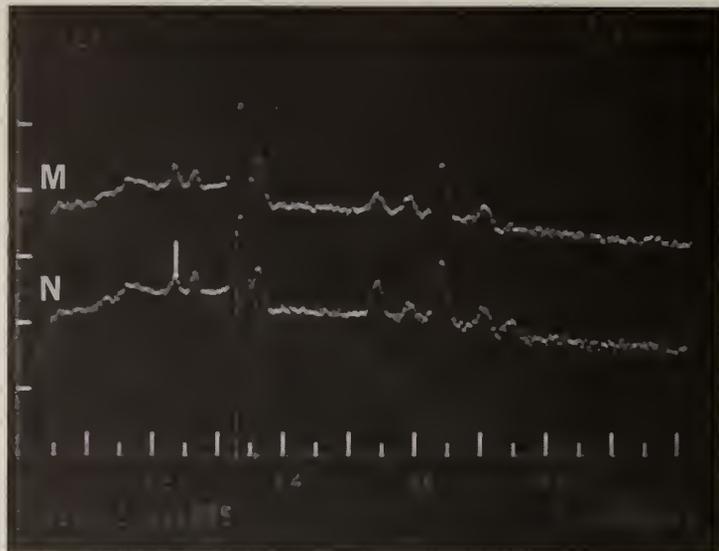
Fig. 11.   EDX spectra of regions M and N of Fig. 4 showing high K concentration.
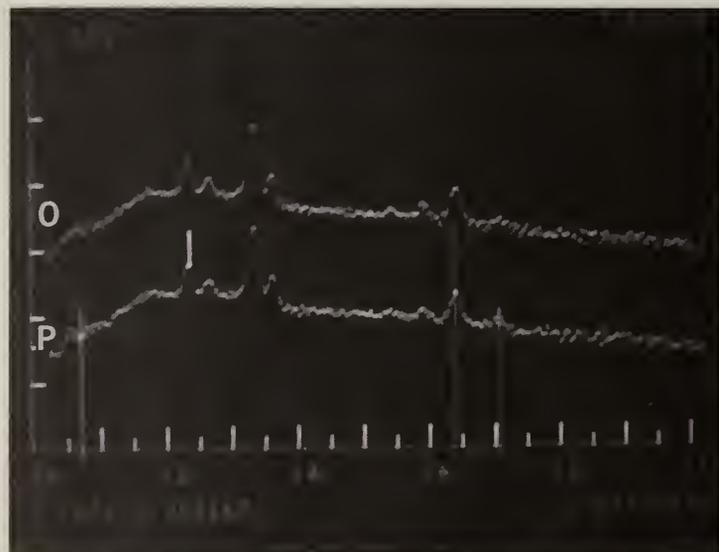
Fig. 12.   EDX spectra of regions O and P of Fig. 4 showing Fe and trace Cr
in salt deposit.

Fig. 13   SEM micrograph, 1800 X, of region T of optical micrograph Fig. 1 showing reaction area at drip zone (fume deposit-salt deposit-metal interface). Lettered regions correspond to labeled EDX spectra, Fig. 14-20.

Fig. 14.   EDX spectra of regions A and B of Fig. 13 showing high Cr concentration.
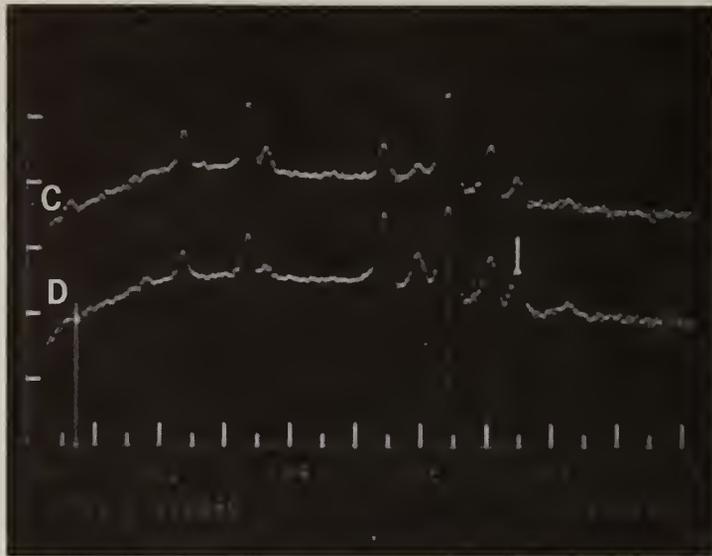
Fig. 15.   EDX spectra of regions C and D of Fig. 13 showing high Cr concentration.
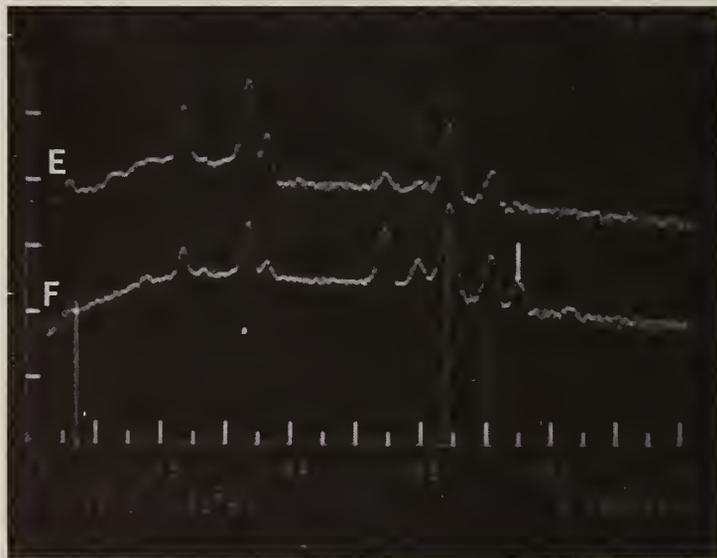
Fig. 16.   EDX spectra of regions E and F of Fig. 13 showing high Cr concentration.
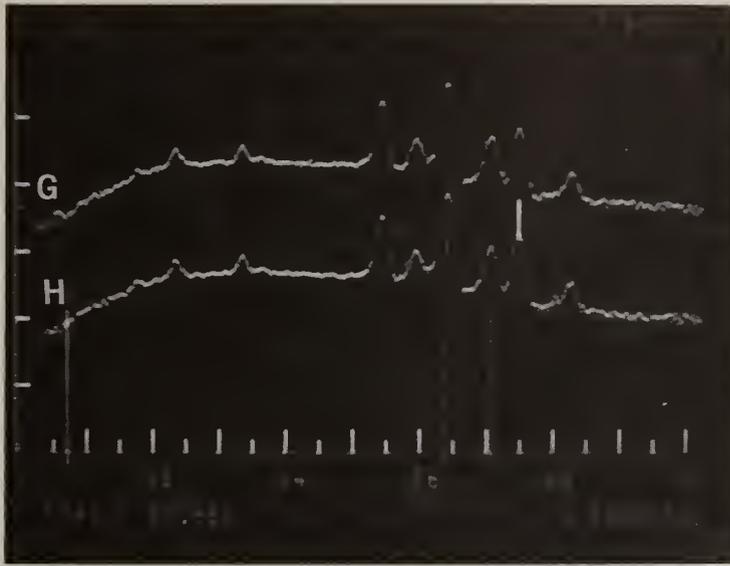
Fig. 17. EDX spectra of regions G and H of Fig. 13 showing high concentrations of both Ni and Cr.
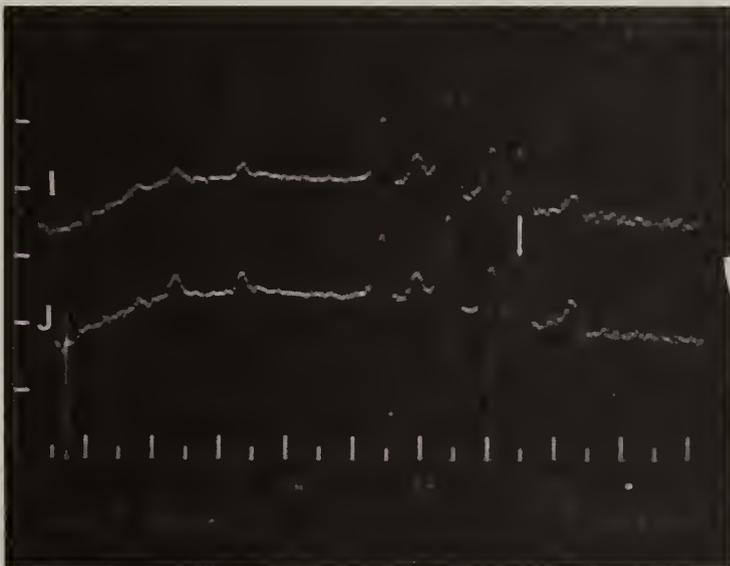
Fig. 18. EDX spectra of regions I and J of Fig. 13 showing high concentrations of both Ni and Cr.
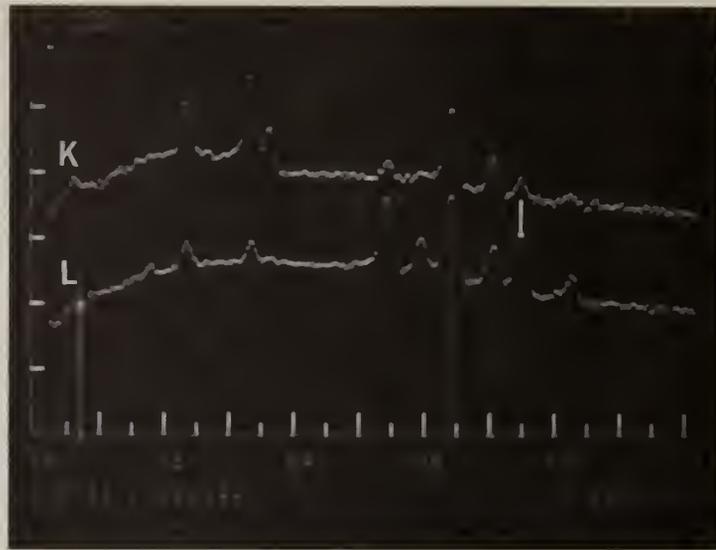
Fig. 19.   EDX spectra of regions K and L of Fig. 13 showing high concentrations of both Ni and Cr.
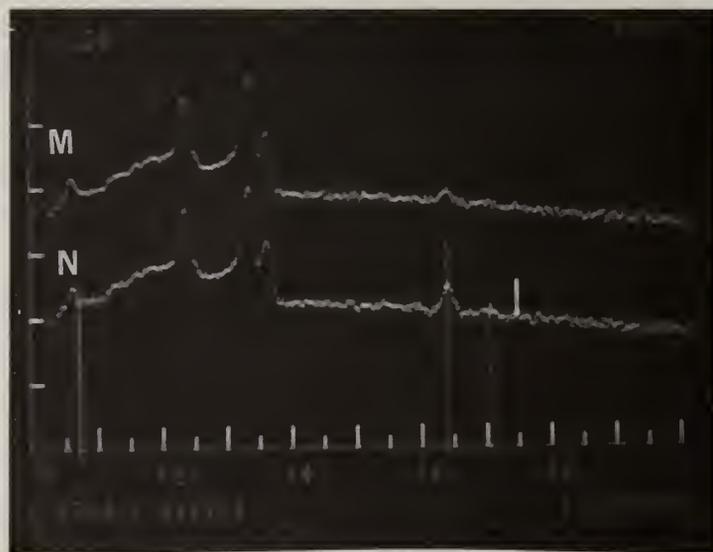
Fig. 20.   EDX spectra of regions M and N of Fig. 13 showing high S and K and a trace of Fe.
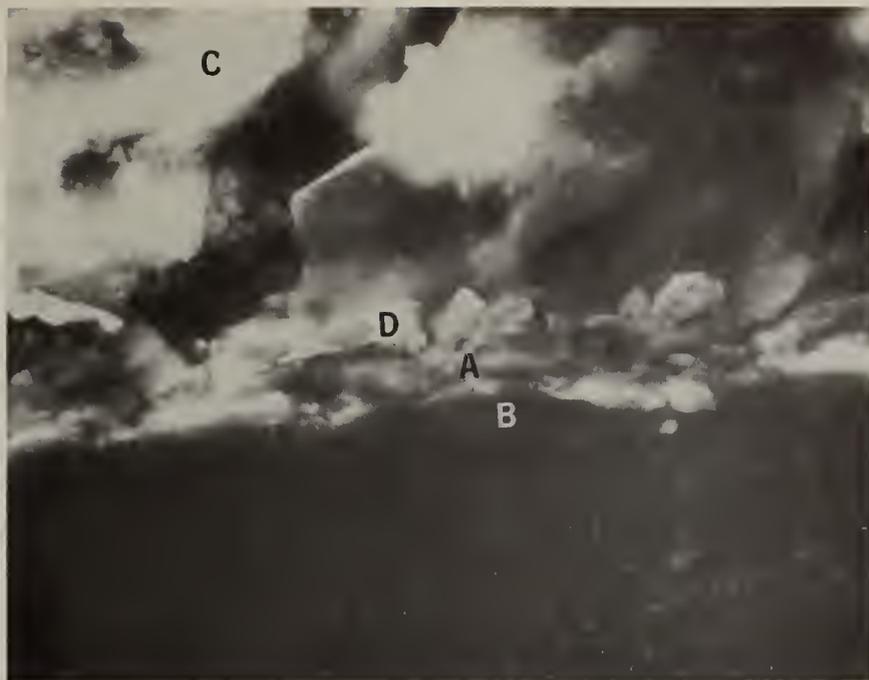
Fig. 21.   SEM micrograph, 1800 X, of region ɣ of optical micrograph Fig. 1 showing
reaction area at metal-fume deposit interface.   Lettered regions corre-
spond to labeled EDX spectra, Fig. 22 and 23.

Fig. 22.   EDX spectra of regions A and B of Fig. 21 showing high Cr concentrations.
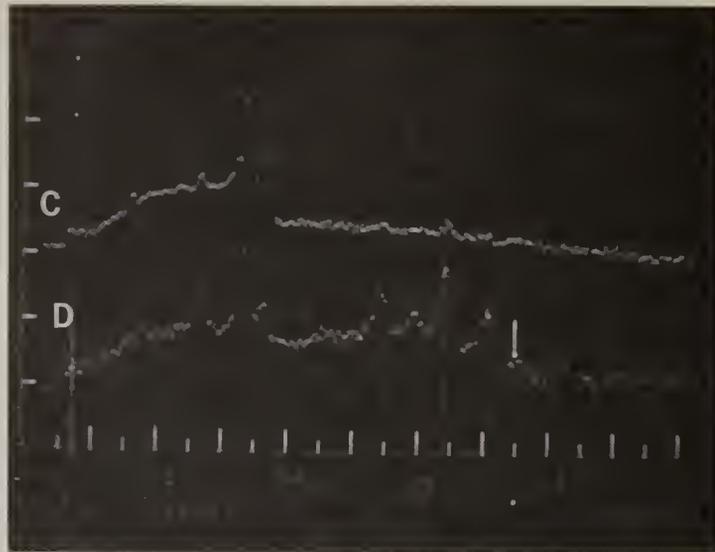
Fig. 23.   EDX spectra of regions C and D of Fig. 21 showing absence of Ni.
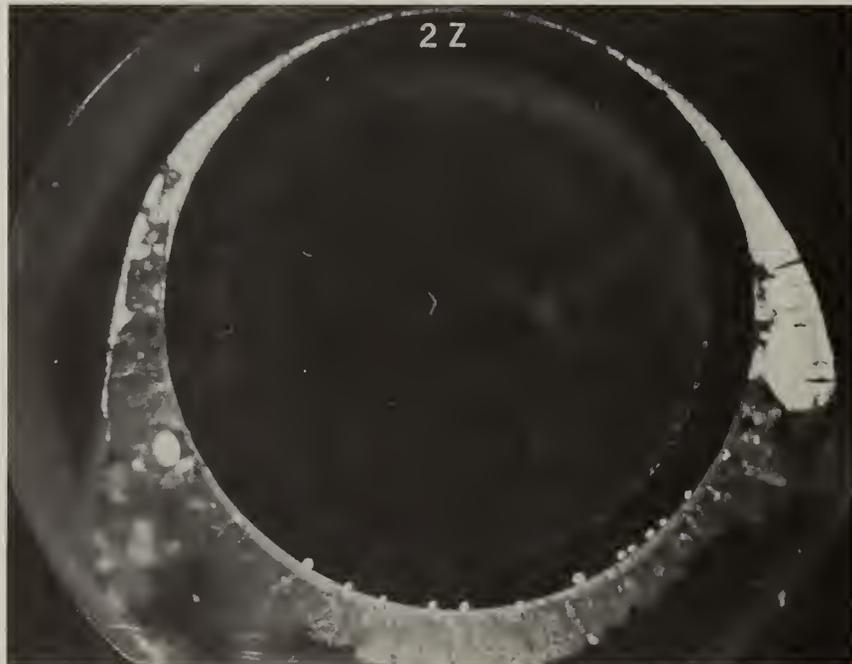
Fig. 24.   Optical micrograph of a section of Type 316 stainless steel tubing after exposure to a fuel rich hot gas stream seeded with K_2SO_4 and K_2CO_3.   Tube temperature 590°C.   Note deposit on upper surface of tube.
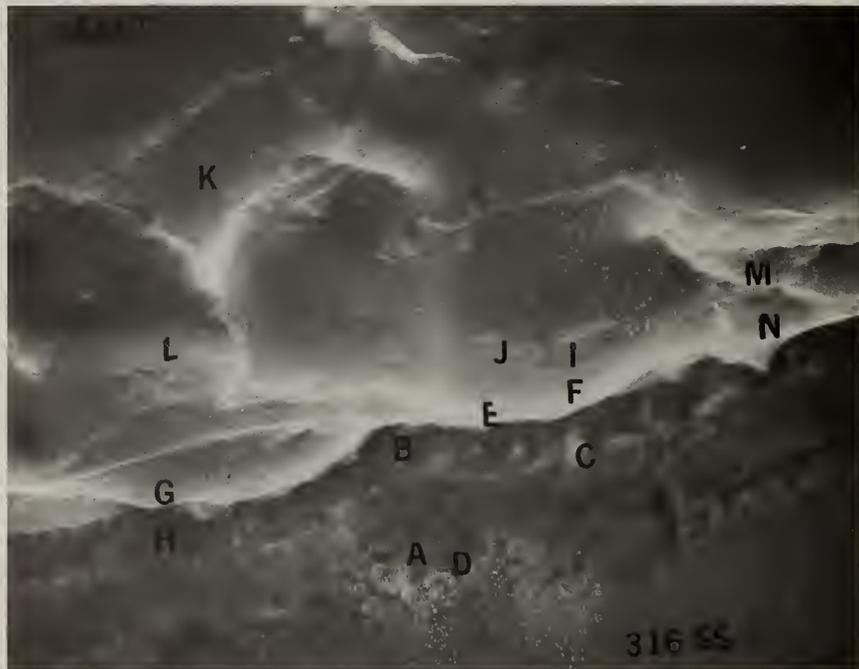
Fig. 25.   SEM micrograph, 1720 X, of region 2Z of optical micrograph Fig. 24
Lettered regions correspond to labeled EDX spectra Fig. 26-34.

Fig. 26.   EDX spectra of regions A and B of Fig. 25 showing high Cr and Ni con-
centrations.
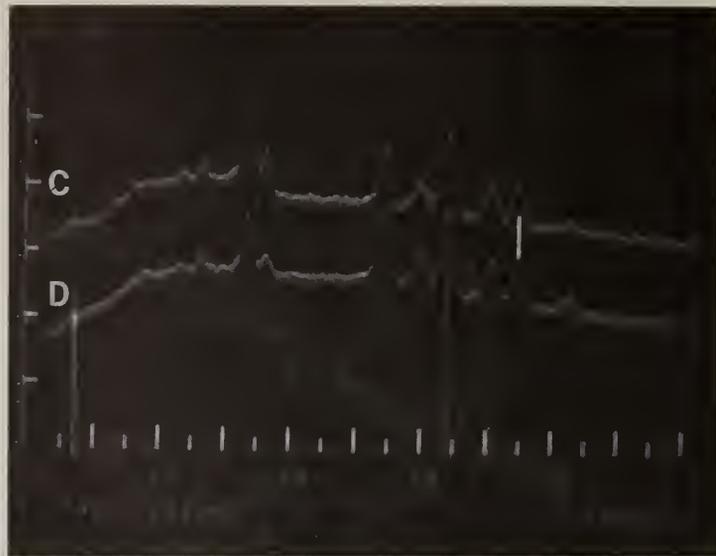
Fig. 27. EDX spectra of regions C and D of Fig. 25 showing high Cr and Ni concentrations.
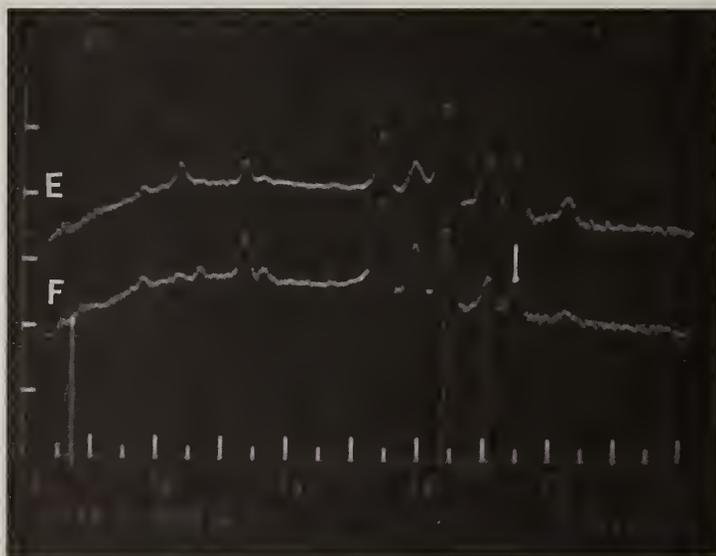
Fig. 28. EDX spectra of regions E and F of Fig. 25 showing high Cr concentrations.

Fig. 29.   EDX spectra of regions G and H of Fig. 25 showing high Cr con-
            centrations.

Fig. 30.   EDX spectra of regions I and J of Fig. 25 showing high Fe con-
            centrations.
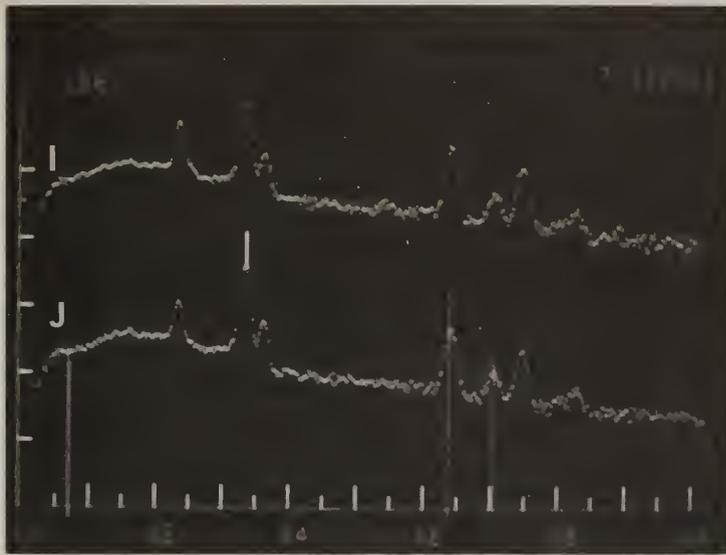
Fig. 31.　EDX spectra of regions K and L of Fig. 25 showing high Fe concentrations.
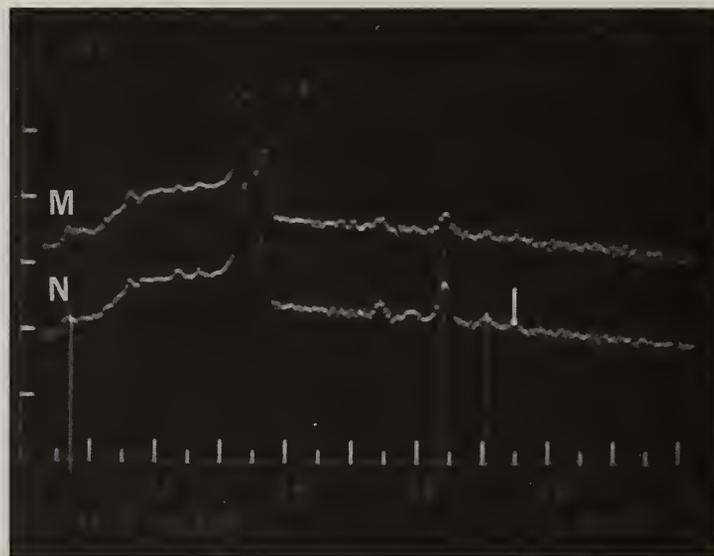
Fig. 32.　EDX spectra of regions M and N of Fig. 25 showing Fe.
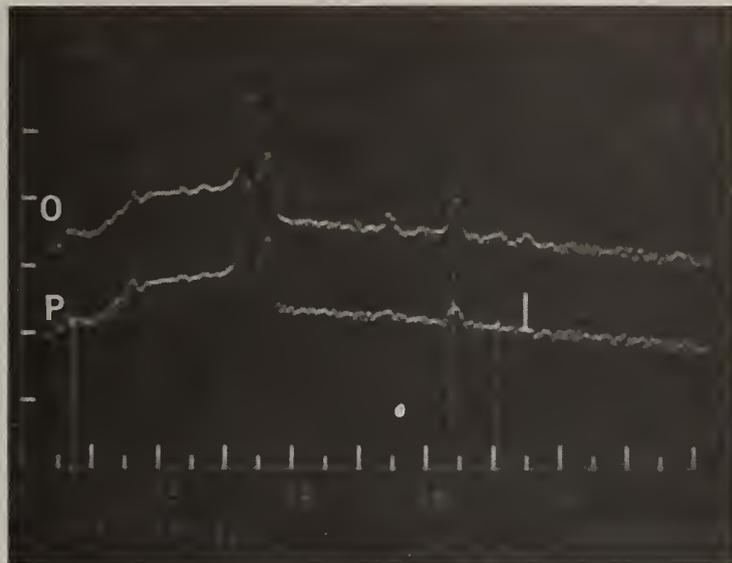
Fig. 33.   EDX spectra of regions O and P of Fig. 25 showing trace of Fe
in the salt deposit.
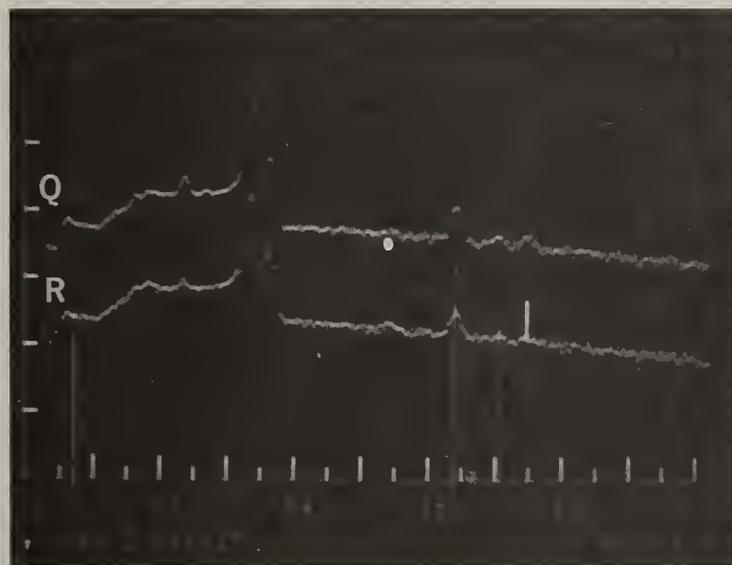
Fig. 34.   EDX spectra of regions Q and R of Fig. 25 showing trace of Fe
in the salt deposit.
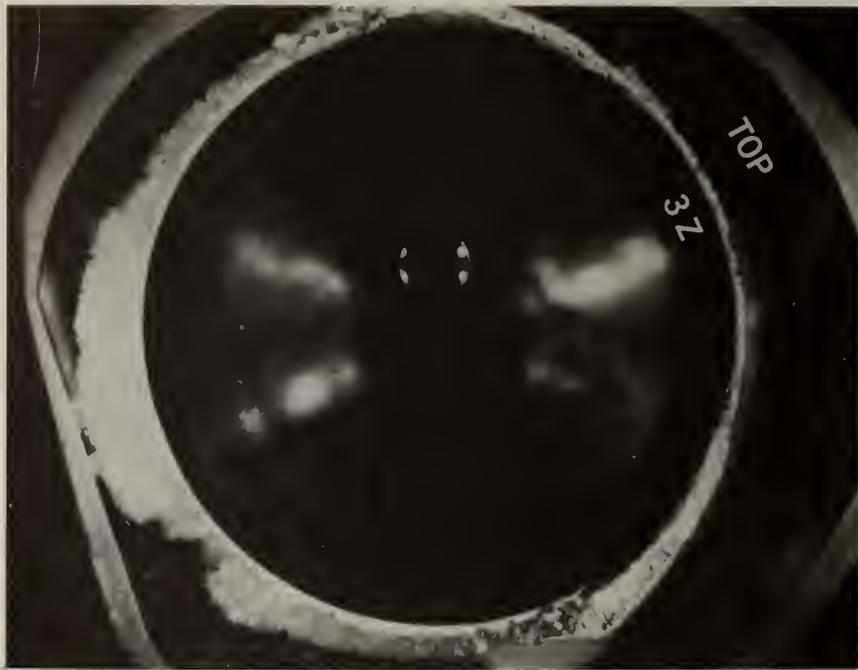
Fig. 35.   Optical micrograph of a section of Type 316 stainless steel tubing after exposure to a fuel rich hot gas stream seeded with K_2SO_4. Tube wall temperature 590°C. Note deposit on upper surface of tube.

Fig. 36.   SEM micrograph, 1720 X, of region 3Z of optical micrograph, Fig. 35. Lettered regions correspond to labeled EDX spectra Fig. 37-43.
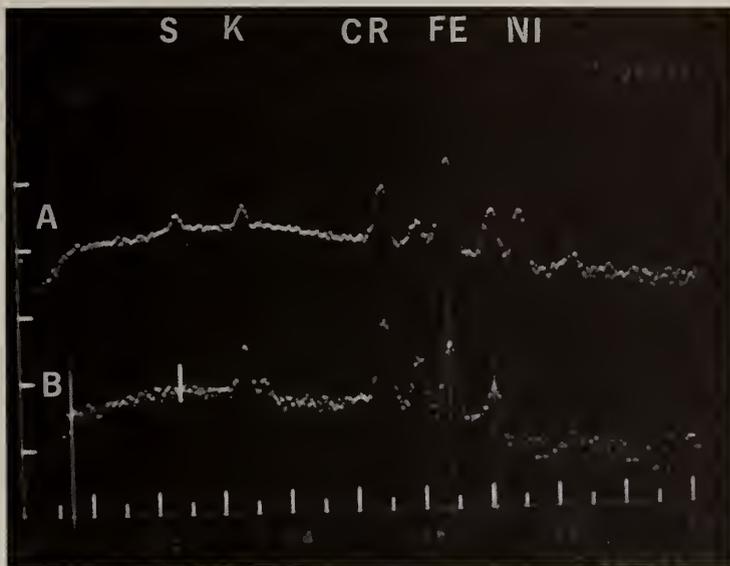
Fig. 37.   EDX spectra of regions A and B of Fig. 36 showing high concentrations of Cr and absence of Ni.
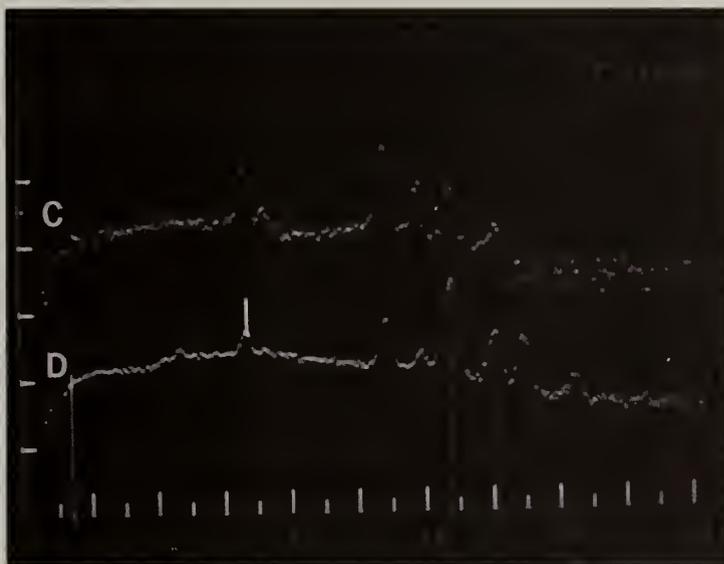
Fig. 38.   EDX spectra of regions C and D of Fig. 36 showing high concentrations of Cr and absence of Ni.
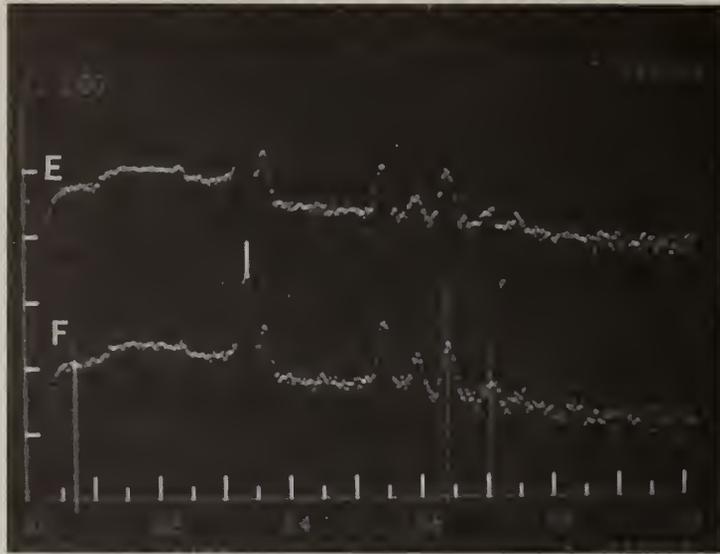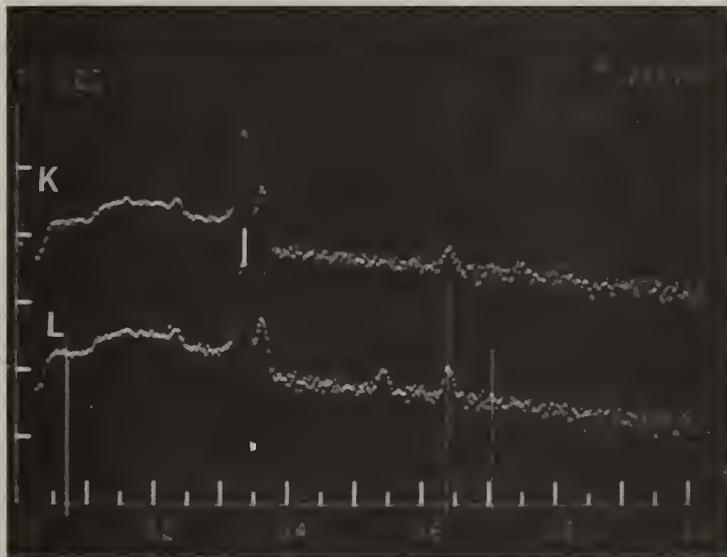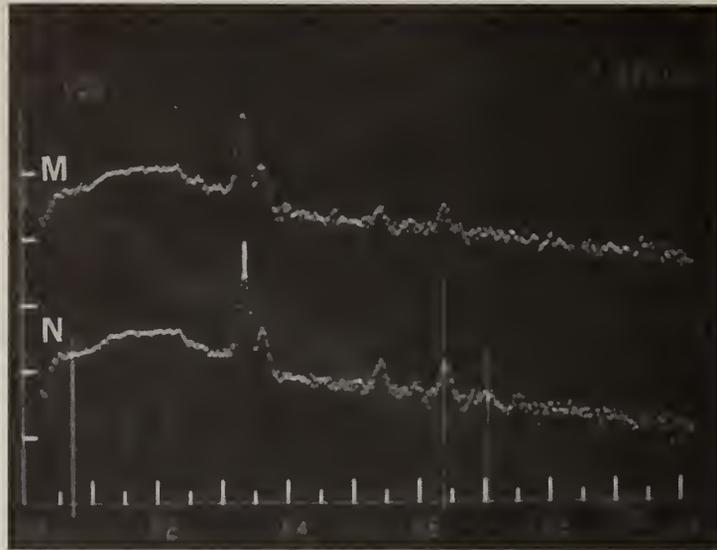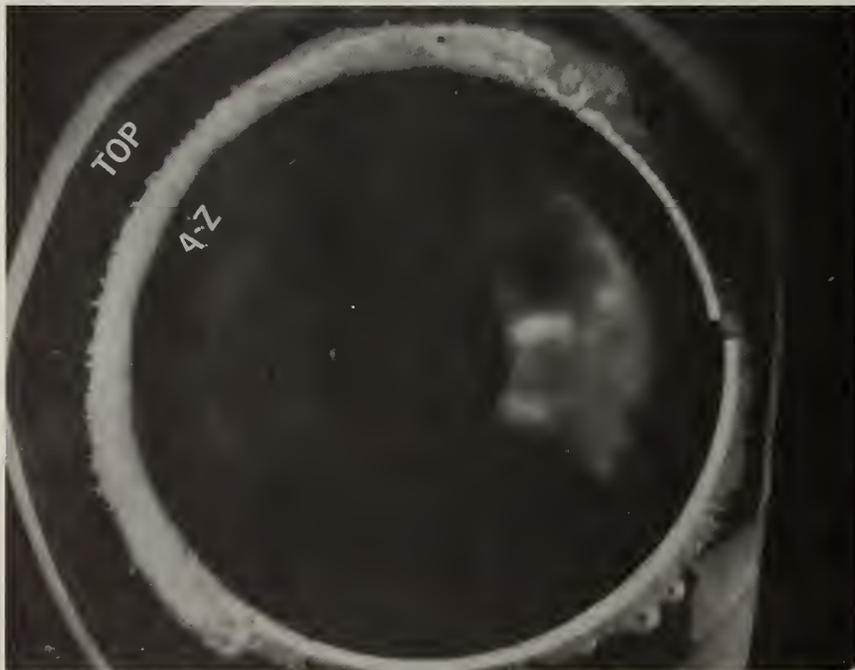
Fig. 39.   EDX spectra of regions E and F of Fig. 36 showing high concentrations of Cr and absence of Ni.
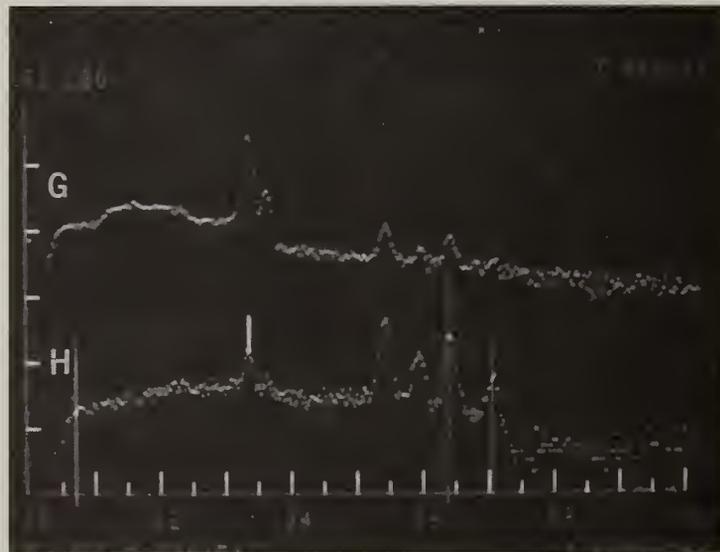
Fig. 40.   EDX spectra of regions G and H of Fig. 36 showing high concentrations of Cr and absence of Ni.

40

Fig. 41.   EDX spectra of regions I and J of Fig. 36 showing high concentrations of Ni and absence of Cr.

Fig. 42.   EDX spectra of regions K and L of Fig. 36 showing high concentrations of K with a trace of Fe and Cr.

Fig. 43.   EDX spectra of regions M and N of Fig. 36 showing high concentrations of K with a trace of Fe and Cr.

Fig. 44.   Optical micrograph of a section of Type 316 stainless steel tubing after exposure to a fuel rich hot gas stream seeded with K_2SO_4.   Tube wall temperature 500°C.   Note deposit on upper surface of tube.

42
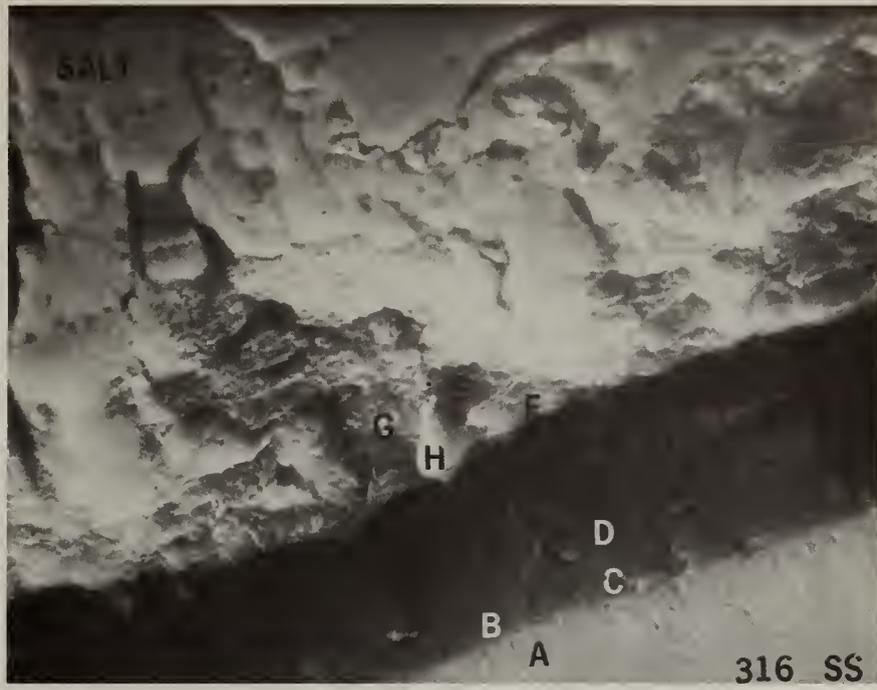
Fig. 45.   SEM micrograph, 1160 X, of region 4Z of optical micrograph Fig. 44
showing reaction area at metal-salt interface.   Lettered regions
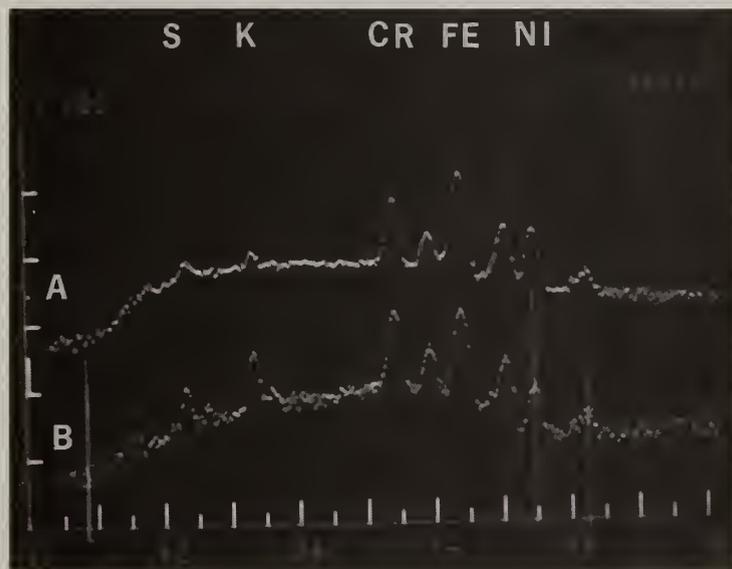correspond to labeled EDX spectra Fig. 46-49.

Fig. 46.   EDX spectra of regions A and B of Fig. 45 showing high Cr and low Ni
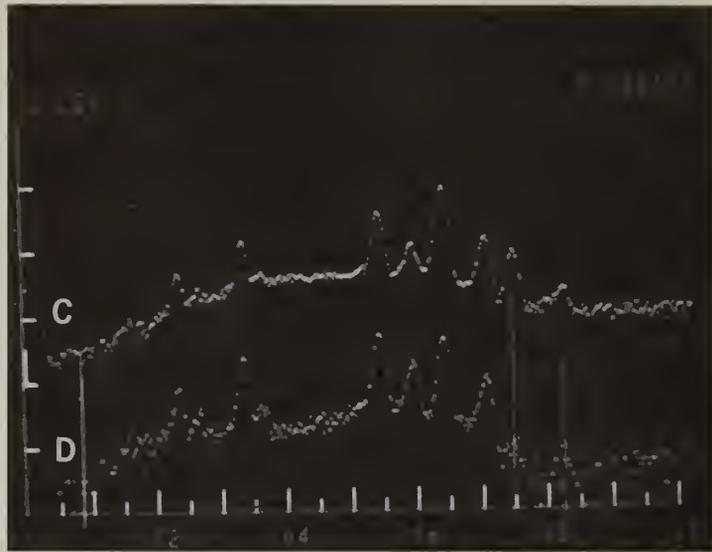concentrations.

Fig. 47.   EDX spectra of regions C and D of Fig. 45 showing high Cr and no Ni.
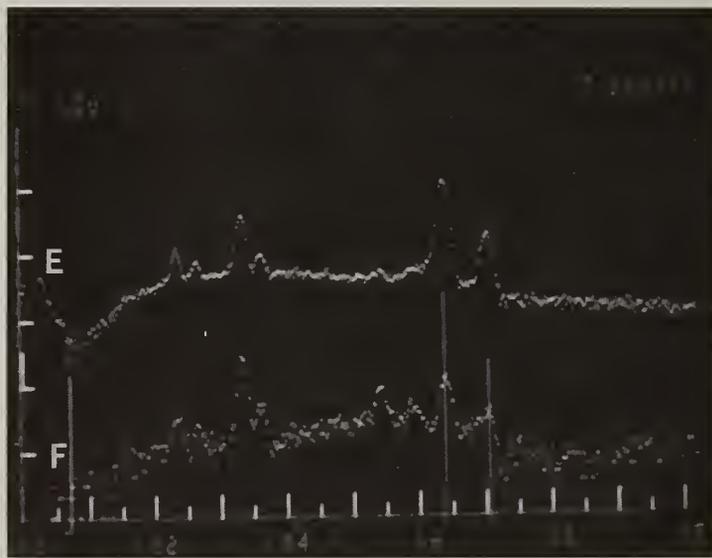

Fig. 48.   EDX spectra of regions E and F of Fig. 45 showing high concentrations
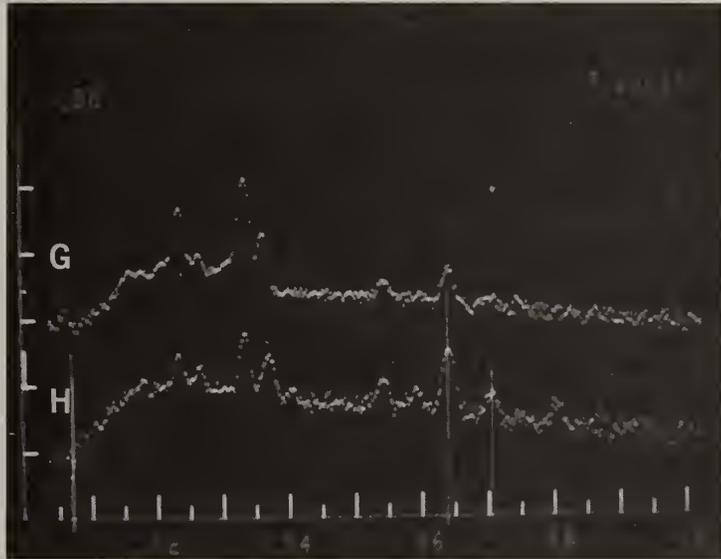   of Fe with a slight trace of Cr.

Fig. 49.   EDX spectra of regions G and H of Fig. 45 showing Fe with a trace of Cr.